

RD-A189 343

STUDIES OF MSFVM (MAGNETOSTATIC FORWARD VOLUME WAVE) TO 1/1

MSBVW (MAGNETOSTA (U) STATE UNIV OF NEW YORK AT STONY

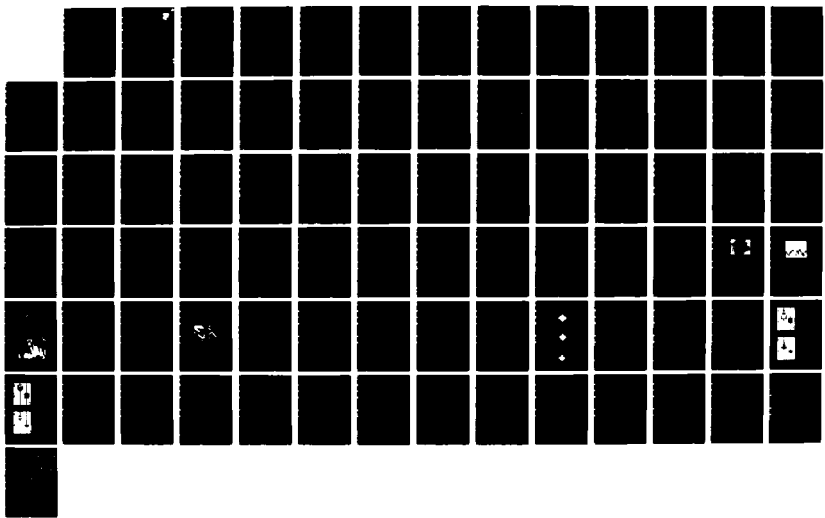
BROOK DEPT OF ELECTRICAL ENGI J P PAREKH ET AL

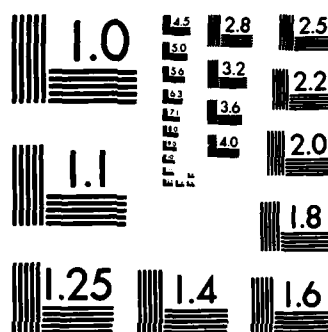
UNCLASSIFIED

DEC 87 RADC-TR-87-201 F19628-82-K-0889

F/G 9/1

NL





MICROCOPY RESOLUTION TEST CHART  
NATIONAL BUREAU OF STANDARDS-1963-A

AD-A189 343

RADC-TR-87-201  
Final Technical Report  
December 1987

DTIC FILE COPY



# **STUDIES OF MSFW TO MSBVW MODE CONVERSION AT A REGION OF BIAS-FIELD DISCONTINUITY AND OF THE DISPERSION OF AN MSFW PULSE**

**State University of New York at Stony Brook**

**J. P. Parekh and H. S. Tuan**

*APPROVED FOR PUBLIC RELEASE; DISTRIBUTION UNLIMITED.*

DTIC  
SELECTED  
JAN 26 1988  
S E C T E

**ROME AIR DEVELOPMENT CENTER  
Air Force Systems Command  
Griffiss Air Force Base, NY 13441-5700**

88 1 19 088

This report has been reviewed by the RADC Public Affairs Office (PA) and is releasable to the National Technical Information Service (NTIS). At NTIS it will be releasable to the general public, including foreign nations.

RADC-TR-87-201 has been reviewed and is approved for publication.

APPROVED:

*James C. Sethares*

JAMES C. SETHARES  
Project Engineer

APPROVED:

*John K. Schindler*

JOHN K. SCHINDLER  
Acting Director of Electromagnetics

FOR THE COMMANDER:

*James W. Hyde III*

JAMES W. HYDE III  
Directorate of Plans & Programs

If your address has changed or if you wish to be removed from the RADC mailing list, or if the addressee is no longer employed by your organization, please notify RADC (EEAC) Griffiss AFB NY 13441-5700. This will assist us in maintaining a current mailing list.

Do not return copies of this report unless contractual obligations or notices on a specific document require that it be returned.

## UNCLASSIFIED

SECURITY CLASSIFICATION OF THIS PAGE

Form Approved  
OMB No. 0704-0188

REPORT DOCUMENTATION PAGE			
1a. REPORT SECURITY CLASSIFICATION <b>UNCLASSIFIED</b>		1b. RESTRICTIVE MARKINGS <b>N/A</b>	
2a SECURITY CLASSIFICATION AUTHORITY <b>N/A</b>		3. DISTRIBUTION/AVAILABILITY OF REPORT <b>Approved for public release; distribution unlimited</b>	
2b DECLASSIFICATION/DOWNGRADING SCHEDULE <b>N/A</b>		5. MONITORING ORGANIZATION REPORT NUMBER(S) <b>RADC-TR-87-201</b>	
4 PERFORMING ORGANIZATION REPORT NUMBER(S) <b>N/A</b>		7a. NAME OF PERFORMING ORGANIZATION <b>State University of New York at Stony Brook</b>	
6c. ADDRESS (City, State, and ZIP Code) <b>Department of Electrical Engineering Stony Brook NY 11794</b>		6b. OFFICE SYMBOL (If applicable) <b>NE</b>	
7b. ADDRESS (City, State, and ZIP Code) <b>Hanscom AFB MA 01731-5000</b>		7a. NAME OF MONITORING ORGANIZATION <b>Rome Air Development Center (EEAC)</b>	
8a. NAME OF FUNDING/SPONSORING ORGANIZATION <b>AFOSR</b>		8b. OFFICE SYMBOL (If applicable) <b>NE</b>	
8c. ADDRESS (City, State, and ZIP Code) <b>Bolling AFB DC 20332-6448</b>		9. PROCUREMENT INSTRUMENT IDENTIFICATION NUMBER <b>F19628-82-K-0009</b>	
10. SOURCE OF FUNDING NUMBERS		PROGRAM ELEMENT NO <b>61102F</b>	PROJECT NO. <b>2305</b>
		TASK NO <b>J5</b>	WORK UNIT ACCESSION NO <b>33</b>
11. TITLE (Include Security Classification) <b>STUDIES OF MSFVW TO MSBVW MODE CONVERSION AT A REGION OF BIAS-FIELD DISCONTINUITY AND OF THE DISPERSION OF AN MSFVW PULSE</b>			
12. PERSONAL AUTHOR(S) <b>J.P. Parekh, H.S. Tuan</b>			
13a. TYPE OF REPORT <b>Final</b>	13b. TIME COVERED <b>FROM Aug 82 TO May 87</b>	14. DATE OF REPORT (Year, Month, Day) <b>December 1987</b>	15. PAGE COUNT <b>84</b>
16. SUPPLEMENTARY NOTATION <b>N/A</b>			
17. COSATI CODES		18. SUBJECT TERMS (Continue on reverse if necessary and identify by block number)	
FIELD <b>20</b>	GROUP <b>14</b>	Microwave <b>Magnetostatic Waves</b>	
FIELD <b>09</b>	GROUP <b>01</b>	Ferrites <b>Delay Lines</b>	
19. ABSTRACT (Continue on reverse if necessary and identify by block number)			
<p>This report investigates mode conversion from magnetostatic forward volume waves (MSFVW's) to magnetostatic backward volume waves (MSBVW's) through a region of bias-field discontinuity and the prospects of monolithically implementing a nondispersive delay line on a given YIG-film strip by changing the magnitude and direction of the internal bias field within the delay line between the two microstrip transducers so that a portion of the delay would support MSFVW and the remainder of the delay line would support MSBVW. This configuration constitutes a monolithic implementation of a discrete forward wave-type delay line cascaded to a discrete backward wave-type delay line, with the requisite dispersion self-compensation achieved by matching the delay characteristics of the two delay lines.</p> <p>The principle objective was to establish if efficient mode conversion is possible over a wide bandwidth. The problem was attacked by performing theoretical and experimental studies simultaneously. The experimental study indicated the presence of mode conversion only (over)</p>			
20. DISTRIBUTION/AVAILABILITY OF ABSTRACT <input checked="" type="checkbox"/> UNCLASSIFIED/UNLIMITED <input type="checkbox"/> SAME AS RPT <input type="checkbox"/> DTIC USERS		21. ABSTRACT SECURITY CLASSIFICATION <b>UNCLASSIFIED</b>	
22a. NAME OF RESPONSIBLE INDIVIDUAL <b>James C. Sethares</b>		22b. TELEPHONE (Include Area Code) <b>(617) 377-4663</b>	22c. OFFICE SYMBOL <b>RADC (EEAC)</b>

UNCLASSIFIED

Block 19. Abstract (Cont'd)

over a very narrow band. Initial theoretical results for mode conversion across a single boundary separating two regions with fixed bias-field angles were encouraging in that they showed that, for a small change of tilt angle across the boundary, efficient mode conversion is possible over a wide band.

The theory of mode conversion was extended to a practical geometry with a gradual bias-field discontinuity region. This geometry was modeled as a segmented or layered geometry along the length of the discontinuity region, i.e., it was approximated by a number of tilted bias-field layers or regions, with the bias-field orientation or tilt angle being constant within each region and varying slowly from one region to the next. Theoretical computations on mode conversion through the layered structure predicted the existence of a MSW cut-off condition. A careful look at the implications of this cut-off condition led to the conclusion that mode conversion from MSFVW to MSBVW in going through a gradual bias-field discontinuity region is theoretically not possible, implying narrow band conversion only.



Accession For	
NTIS GRA&I	<input checked="" type="checkbox"/>
DTIC TAB	<input type="checkbox"/>
Unannounced	<input type="checkbox"/>
Justification	
By _____	
Distribution/	
Availability Codes	
Dist	Avail and/or Special
A-1	

UNCLASSIFIED

**Table of Contents**

<b>Summary .....</b>	<b>1</b>
<b>Chapter 1: MSVW-to-MSBVW mode conversion at a region of bias</b>	
<b>field discontinuity .....</b>	<b>3</b>
<b>1.1. Introduction .....</b>	<b>3</b>
<b>1.2. Theory .....</b>	<b>7</b>
<b>1.2.1. Free MSVW modes of a YIG film with internal</b>	
<b>bias field lying in an arbitrary direction in</b>	
<b>the sagittal plane .....</b>	<b>11</b>
<b>1.2.2. MSVW mode conversion in a single-interface</b>	
<b>geometry .....</b>	<b>18</b>
<b>1.2.2.1. Problem Formulation .....</b>	<b>18</b>
<b>1.2.2.2. Computed mode conversion characteristics .....</b>	<b>20</b>
<b>1.2.3. MSVW scattering at a region of gradual bias-field</b>	
<b>discontinuity .....</b>	<b>29</b>
<b>1.2.3.1. Scattering matrix for a single sub-region based</b>	
<b>on three-mode-coupling formalism .....</b>	<b>29</b>
<b>A. Scattering matrix for a single interface .....</b>	<b>33</b>
<b>B. Scattering matrix for transmission line .....</b>	<b>37</b>
<b>C. Scattering matrix for a single sub-region .....</b>	<b>37</b>

1.2.3.2. Scattering-matrix formalism for the transition region based on three-mode-coupling model .....	39
1.2.3.3. Generalized multi-mode coupling formalism for the transition region .....	40
1.3. Experimental work .....	45
1.4. New theoretical developments .....	51
1.5. Conclusions .....	53
Chapter 2: Dispersion of a time-limited MSFVW CW pulse .....	54
2.1. Introduction .....	54
2.2. Basic theory of pulse dispersion .....	55
2.3. Numerical results .....	56
2.4. Experimental results .....	59
2.5. Conclusion .....	59

## SUMMARY

The original goal of the present contract was (i) to study the properties of mode conversion from magnetostatic forward volume waves (MSFVW's) to magnetostatic backward volume waves (MSBVW's) through a region of bias-field discontinuity, and then (ii) to investigate the prospects of *monolithically* implementing a *nondispersive* delay line on a given YIG-film strip by changing the magnitude and direction of the internal bias field within the delay line between the two microstrip transducers so that a portion of the delay line would support MSFVW and the remainder of the delay line would support MSBVW. This configuration constitutes a monolithic implementation of the Sethares *et al* geometry [1] wherein a *discrete* forward wave-type delay line was cascaded to a *discrete* backward wave-type delay line, with the requisite dispersion self-compensation achieved by matching the delay characteristics of the two delay lines.

A detailed study of MSFVW-to-MSBVW mode conversion through a region of bias-field discontinuity is described in Chapter 1. The principal objective of this study was to establish if *efficient* mode conversion is possible over a *wide* bandwidth. The problem was attacked by performing theoretical and experimental studies simultaneously. The experimental study indicated the presence of mode conversion but this conclusion was somewhat ambiguous because of the rather unsophisticated nature of the biasing magnet circuit employed and the consequent lack of definition of the profile of the internal bias field along the length of the delay line. Initial theoretical results for mode conversion across a single boundary separating two regions with fixed bias-field angles were encouraging in that they showed that, for a small change of tilt angle across the boundary, efficient mode conversion is possible over a *wide* band.

The theory of mode conversion was successfully extended to a practical geometry with a gradual bias-field discontinuity region. This geometry was modeled as a

segmented or layered geometry along the length of the discontinuity region, i.e., it was approximated by a number of tilted bias-field layers or regions, with the bias-field orientation or tilt angle being constant within each region and varying slowly from one region to the next. While this work was being performed, a sophisticated magnet system providing precision bias-field change over the length of a YIG film sample was being designed. At this time, the theoretical computations on mode conversion through the layered structure ran into a snag which was ultimately traced to the existence of the unique MSW cut-off condition. A careful look at the implications of this cut-off condition led to the catastrophic conclusion that mode conversion from MSFVW to MSBVW in going through a bias-field discontinuity region is theoretically *not* possible.

The foregoing turn of events led to a termination of the effort on MSFVW to MSBVW mode conversion in going through a region of bias-field discontinuity region. The effort during the remainder of the contract period was dedicated to a characterization of the dispersion of an MSFVW pulse suffered during propagation. This study was successfully performed using Fast Fourier Transform techniques and is described in Chapter 2.

## CHAPTER 1

### MSFVW-to-MSBVW MODE CONVERSION AT A REGION OF BIAS FIELD DISCONTINUITY

#### 1.1. INTRODUCTION

The present chapter describes theoretical and experimental work performed on the subject of MSFVW to MSBVW mode conversion that one expects to occur when an MSFVW is incident at a region of bias-field discontinuity separating a region with bias field normal to the YIG film (the MSFVW region) from a region with bias field parallel to the YIG film and to the direction of MSW propagation (the MSBVW region). This study was undertaken to establish that the expected *efficient* mode conversion is indeed possible over a *wide* bandwidth with such a scheme. The aim of the contract was to proceed, after establishing the existence of efficient MSFVW-to-MSBVW mode conversion through a suitably profiled bias-field discontinuity region, to a *monolithic* implementation of a *nondispersive* MSW delay line wherein, within a single delay line, part of the delay line supports MSFVW propagation and the remaining delay line supports MSBVW propagation, thereby permitting a mechanism for achieving dispersion self-compensation. The latter geometry constitutes a *monolithic* implementation of the Sethares *et al* [1] *nondispersive* MSW delay line geometry which consisted of two cascaded *discrete* delay lines, one being a forward wave-type (MSSW or MSFVW) delay line and the other a backward wave-type (MSBVW) delay line.

After establishing the existence of efficient mode conversion over a wide bandwidth, the question of achieving dispersion self-compensation may then be handled in the manner it was handled in the Sethares *et al* cascaded geometry of discrete delay lines, i.e., through the use of appropriately spaced ground planes (and the possible use of multi-layered YIG films [2]). Some theoretical work performed under partial support

from the present contract [2] (see Attachment A) has shown that superior nondispersive MSFVW characteristics may be achieved by using a layered-YIG-film in conjunction with a spaced ground plane. The dispersion self-compensation is not treated in the present report.

The theoretical work evolved over three phases. In the first phase, a theory for MSFVW-to-MSBVW mode conversion was worked out for the case of an *abrupt* bias-field discontinuity. The choice of abrupt bias-field discontinuity was based on the fact that this represents the simplest geometry and the consequent expectation that this choice might yield the simplest approach at handling the complex problem of mode conversion. While, in this theory, an incident fundamental-mode MSFVW was considered to scatter into all MSFVW reflected modes and all MSBVW transmitted modes, it was shown that the resulting infinite set of equations in the unknown amplitude coefficients could be truncated depending on the level of accuracy desired in evaluating the coupling coefficients. It was found, in agreement with what one might expect, that the modes that need to be included in the truncation are the ones that are *phase-matched* to the chosen incident mode along the direction normal to the YIG film at the boundary separating the MSFVW and MSBVW regions. It was recognized that, in addition to the multi-moded nature of mode conversion, most of the incident power is reflected back, a feature that reflects the abrupt nature of impedance discontinuity at the junction plane.

Based on the work performed during the first theoretical phase, it became evident that efficient mode conversion into a *single* mode required that the bias-field discontinuity be sufficiently *gradual* so that the transverse phase-matching to the incident mode is possible with essentially a single converted mode.

An extended gradual bias-field discontinuity region may be approximated by a segmented or layered geometry comprised of a number of tilted bias-field regions, with the bias-field orientation or tilt angle being constant within each region and varying slowly from one region to the next. In a systematic approach at solving the problem of mode conversion through such a "layered" transition region, one would first solve the problem of mode conversion across a single boundary separating two regions with fixed bias-field tilt angles, with the change of tilt angle across the boundary being small.

The problem of mode conversion across a single boundary was successfully solved for the case of an incident magnetostatic volume wave (MSVW), i.e., for the case of bias field oriented in the sagittal plane [3] (see Attachment B). It was found that, the more gradual the discontinuity, the better is the accuracy in using a *three-mode coupling model* which assumes the coupling of three modes, viz., the incident wave, one reflected wave and one transmitted wave. The computations have shown that efficient mode conversion obtains over a wide band for modes that are phase-matched to the incident wave in the direction normal to the YIG film.

In the third theoretical phase, the three-mode coupling theory was successfully extended to the case of a "layered" transition region sandwiched between two pure-mode regions using a scattering-parameter formalism. In the course of numerical computations, however, irreconcilable difficulties were encountered which were ultimately traced to the unique cut-off phenomenon present in MSW propagation. A careful evaluation of the implications of this cut-off condition led to the catastrophic conclusion that mode conversion from MSVW to MSBVW in going through an extended transition region is theoretically *not* possible.

The experimental portion of the work was focused on the observation of mode conversion in a single straight YIG strip. The experiment employed a 3-transducer

geometry, with the middle transducer placed half-way between the other two transducers being a diagnostic transducer. First the device was set up as an MSSW delay line within an electromagnet and the transmission was measured between the two outer transducers. The choice of MSSW for the forward wave-type portion of the cascaded structure was based on the fact that a smaller bias field is required compared to MSFVW, thereby permitting the use of small ceramic magnets in the experiment and also reducing the interaction between the two magnet systems. The device was then physically withdrawn approximately half-way out of the bias field so that a transmitted signal was observed at the center transducer but no signal was observed at the outer receiving transducer. Next a horse-shoe magnet was placed over the withdrawn region so that the bias field orientation for this region was for MSBVW. A signal was now observed at the outer receiving transducer assumed to represent the converted signal at the bias-field discontinuity region.

The main problem in the experiment is the strong interaction between the two magnet systems because of their proximity, i.e., the introduction of the second magnet produces a strong perturbation of the field due to the first magnet. A precision magnet design providing desired bias fields, in magnitude and direction, in the two pure-mode regions and separated by a gradual discontinuity region was in progress at the time of the catastrophic theoretical discovery that MSFVW to MSBVW mode conversion through a region of bias-field discontinuity is not possible.

While the design of a precision magnet system was awaited, a special magnet circuit was empirically designed and machined as an attachment to the electromagnet pole pieces. The objective of this magnet system was to remove the problem associated with the rather large dimensions of the horse-shoe pole pieces relative to the length of the YIG film.

A jig was designed and machined which permitted the position of the center diagnostic transducer to be variable over most of the length of the YIG film. An important planned diagnostic study utilizing this diagnostic transducer was the measurement of the physical lengths of the forward and backward wave regions as well as the length of the transition region.

## 1.2. THEORY

The abrupt bias-field geometry (Fig. 1) is a special case of the more realistic gradual bias-field geometry (Fig. 2). As a first step in solving the complicated problem of mode conversion in the geometry of Fig. 2, a much more basic problem that would allow a building-block approach was solved. The two-region geometry shown in Fig. 3 is treated first wherein the internal bias fields in the two regions are oriented in the sagittal plane. The building block approach allows the results for the geometry of Fig. 3 to yield the mode-conversion properties of a gradual bias-field discontinuity region since the latter may be approximated by a number of tilted-bias-field regions, with the tilt angle changing slowly from one region to the next as shown in Fig. 2. A synthesis procedure based on a scattering-parameter approach has been employed in generating the results for the gradual bias-field discontinuity geometry from the single-interface geometry.

As a first step in solving the single-interface geometry problem, the properties and field expressions of the free MSVW modes of an infinite YIG film are derived. Then, in solving the single-interface geometry problem (Fig. 3), which assumes a single MSVW mode incident at the boundary separating the two regions with different bias fields in the sagittal plane, one postulates the reflected and transmitted signals to be given by a superposition of an infinite number of eigenmodes of the two respective regions. The unknown amplitude coefficients of these eigenmodes are determined by the mode-

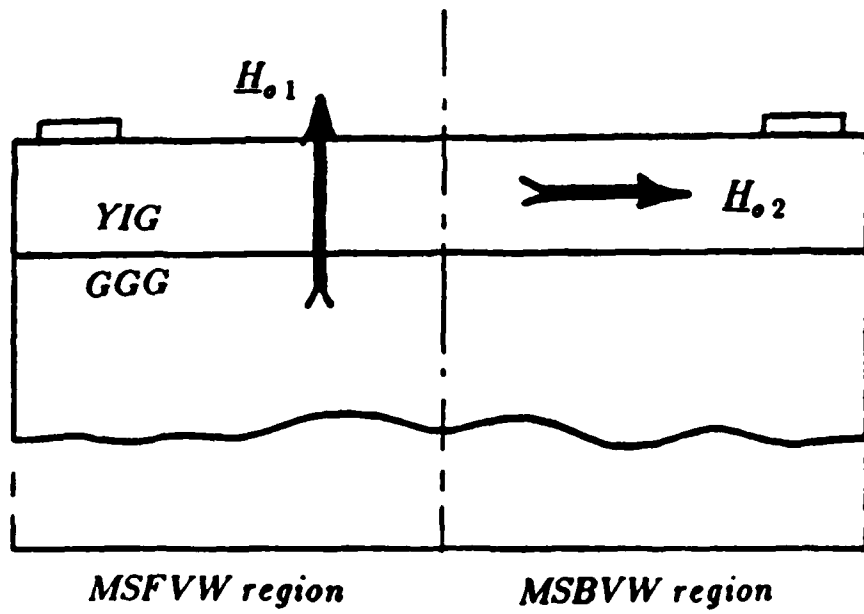


Fig. 1. Abrupt bias-field discontinuity geometry

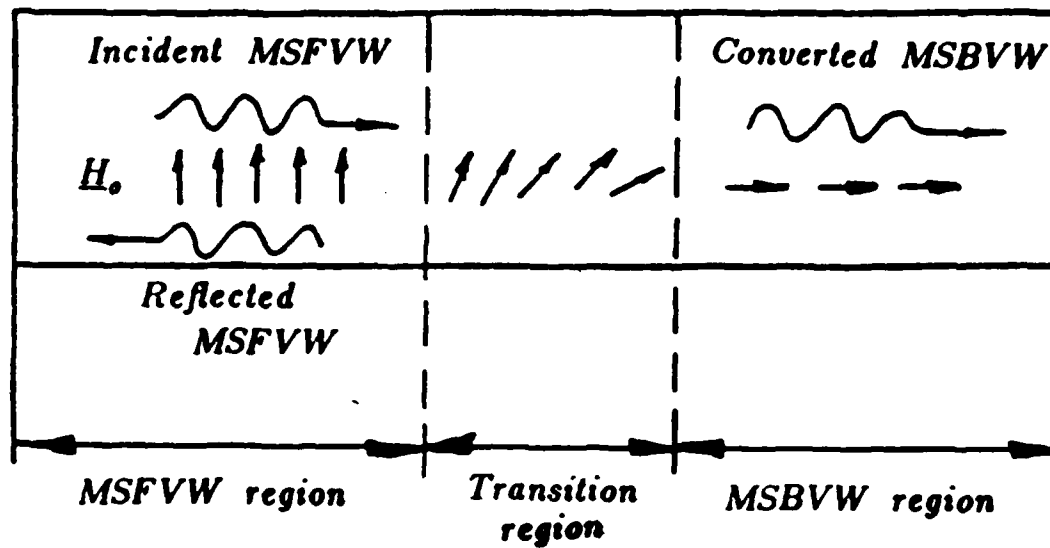


Fig. 2. Gradual bias-field discontinuity geometry

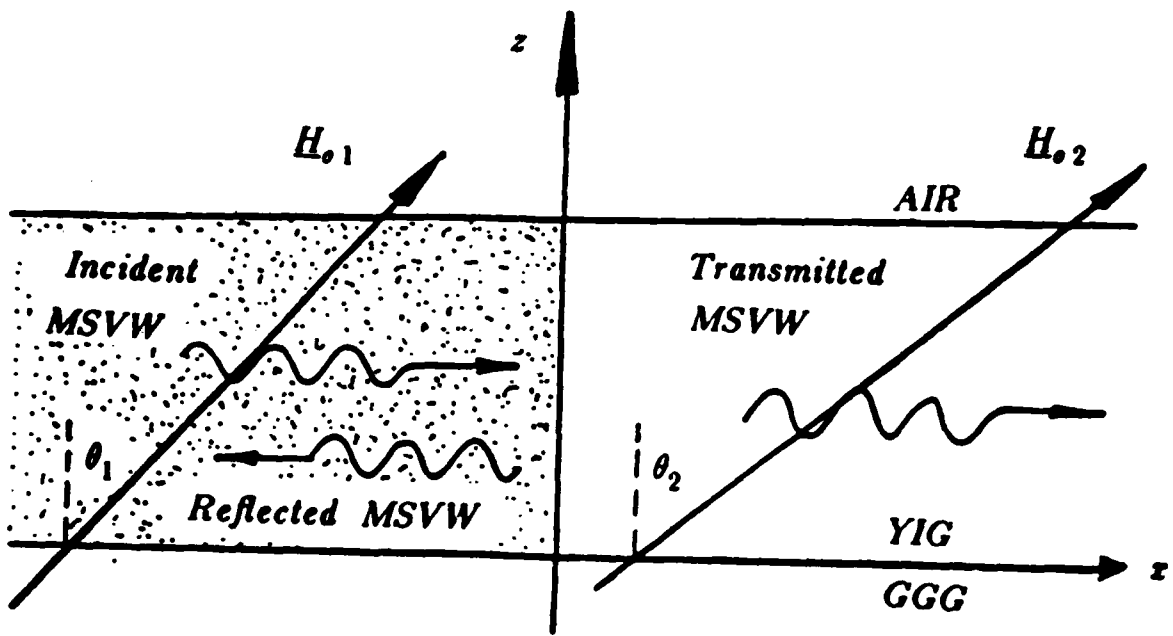


Fig. 3. Single-interface MSVW mode-conversion geometry

matching technique, i.e., by applying boundary conditions at the interface plane and invoking the *bi-orthogonality* [4,5] properties of the eigenmodes.

### 1.2.1. FREE MSW MODES OF A YIG FILM WITH INTERNAL BIAS FIELD LYING IN AN ARBITRARY DIRECTION IN THE SAGITTAL PLANE

The YIG-film geometry with a tilted internal bias field lying in the sagittal plane is shown in Fig. 4. The field expressions for the magnetic potential functions representing the free MSW modes of this infinite film geometry are given by the solutions of the magnetostatic wave equations

$$\left( \frac{\partial^2}{\partial z^2} + \frac{\partial^2}{\partial z^2} \right) \begin{pmatrix} \Phi_{AIR} \\ \Phi_{GGG} \end{pmatrix} = 0$$

$$\left( \mu_3 \frac{\partial^2}{\partial z^2} + 2\mu_{12} \frac{\partial^2}{\partial z \partial z} + \mu_1 \frac{\partial^2}{\partial z^2} \right) \Phi_{NG} = 0 \quad (1)$$

which satisfy the boundary conditions, i.e., the continuity of tangential magnetic field and normal magnetic induction across the interfaces  $z=0$  and  $z=d$ . The potential functions  $\Phi_{AIR}$ ,  $\Phi_{NG}$  and  $\Phi_{GGG}$  representing the air, YIG and GGG regions, respectively, yield the wave rf magnetic fields in the respective regions through the relation  $\mathbf{h} = -\mathbf{grad} \phi$ . The small-signal permeability tensor  $\tilde{\mu}$  for the case of a YIG medium biased beyond saturation by an internal field  $\mathbf{H}$ , lying at an angle  $\theta$  to the  $z$ -axis may be readily shown to be given by

$$\tilde{\mu} = \begin{bmatrix} \mu_1 & -j\mu_{12} & \mu_{13} \\ j\mu_{12} & \mu & -j\mu_{23} \\ \mu_{13} & j\mu_{23} & \mu_3 \end{bmatrix} \quad (2)$$

where

$$\mu_1 = 1 + FC^2$$

$$\mu = 1 + F$$

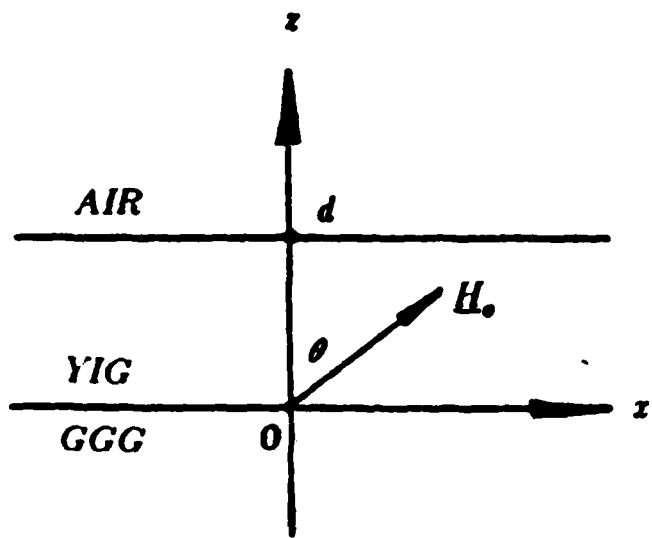


Fig. 4. Infinite YIG-film geometry with arbitrarily oriented bias field in the sagittal plane

$$\begin{aligned}
 \mu_3 &= 1 + FS^2 \\
 \mu_{12} &= \kappa C \\
 \mu_{13} &= -FSC \\
 \mu_{23} &= \kappa S \\
 F &= \frac{f_s f_M}{(f_s^2 - f^2)} \\
 \kappa &= \frac{-f_M f}{(f_s^2 - f^2)} \\
 C &= \cos \theta \\
 S &= \sin \theta
 \end{aligned} \tag{3}$$

The quantities  $f_s, f_s = \gamma\mu_s H_s$ , and  $f_M = \gamma\mu_s M_s$ , are, respectively, the signal, gyro, and magnetization frequencies.

For straight-crested waves propagating along  $z$  direction, i.e.,  $\partial/\partial y = 0$ , the potential functions in the three regions have the expressions

$$\begin{aligned}
 \Phi_{AIR} &= A \rho e^{-|k|(|s-d|)} e^{-jkz} \\
 \Phi_{NG} &= A \left[ e^{js_1 k z} - \frac{(s + j\beta)}{(s - j\beta)} e^{js_2 k z} \right] e^{-jkz} \\
 \Phi_{GGG} &= A \left( \frac{-j2\beta}{s - j\beta} \right) e^{|k|s} e^{-jkz}
 \end{aligned} \tag{4}$$

where

$$\begin{aligned}
 \rho &= \frac{j2\beta(s + j\beta)}{(s - j\beta)^2} e^{js_2 k d} \\
 s_1 &= \frac{(\mu_{13} - \beta)}{\mu_3} \\
 s_2 &= \frac{(\mu_{13} + \beta)}{\mu_3} \\
 \beta &= \sqrt{-\mu}
 \end{aligned} \tag{5}$$

and the propagation wave number is the solution of the dispersion relation

$$\tan\left(\frac{\beta k d}{\mu_3}\right) = \frac{-2\beta s}{(1 + \mu)} \tag{6}$$

The quantity  $s$  has the value  $s=1$  for  $k>0$  and  $s=-1$  for  $k<0$ . The harmonic time dependence  $e^{i\omega t}$  is assumed throughout for all ac quantities.

The transcendental nature of the dispersion relation in Eq. (6) yields an infinite number of modal solutions

$$\left\{ \frac{\beta kd}{\mu_3} \right\}_m = \tan^{-1} \left( \frac{-2\beta s}{1+\mu} \right) + m\pi \quad (7)$$

where  $m$  is a modal index assuming any integer value, i.e.,  $m=0,1,2,3,\dots$ . The dispersion relation (6) and the field expressions (4) reduce correctly to the more commonly used cases corresponding to  $\theta=0^\circ$  and  $\theta=90^\circ$ .

The qualitative features of the MSVW dispersion diagram corresponding to an arbitrary angle  $\theta$  and a given mode are shown in Fig. 5. The overall passband is the frequency range  $f_s < f < f_2$ . Within this passband, the wave is of the forward-wave type for frequencies above  $f_2$ , and of the backward wave-type for frequencies below  $f_2$ . The effect of changing the angle  $\theta$  on the dispersion curve for a given mode is shown in Fig. 6. The dispersion curve correctly reduces to that for the pure MSFVW obtaining for  $\theta=0^\circ$  and to that for the pure MSBVW obtaining for  $\theta=90^\circ$ .

Notice that the negative- $k$  branch is chosen, as it must, to represent the backward-wave solution rather than the usually shown positive- $k$  branch. The negative- $k$  branch corresponds to a positive group velocity and negative phase velocity and is the appropriate one to choose for the geometry of Fig. 3 where the converted MSBVW must carry energy away in the positive- $z$  direction. (While the positive- $k$  branch for MSBVW is a valid solution of the dispersion solution, it represents energy propagation in the negative- $z$  direction and thus does not apply in the present problem.)

The total time-average power carried by the  $m$ th mode in the  $z$  direction is given

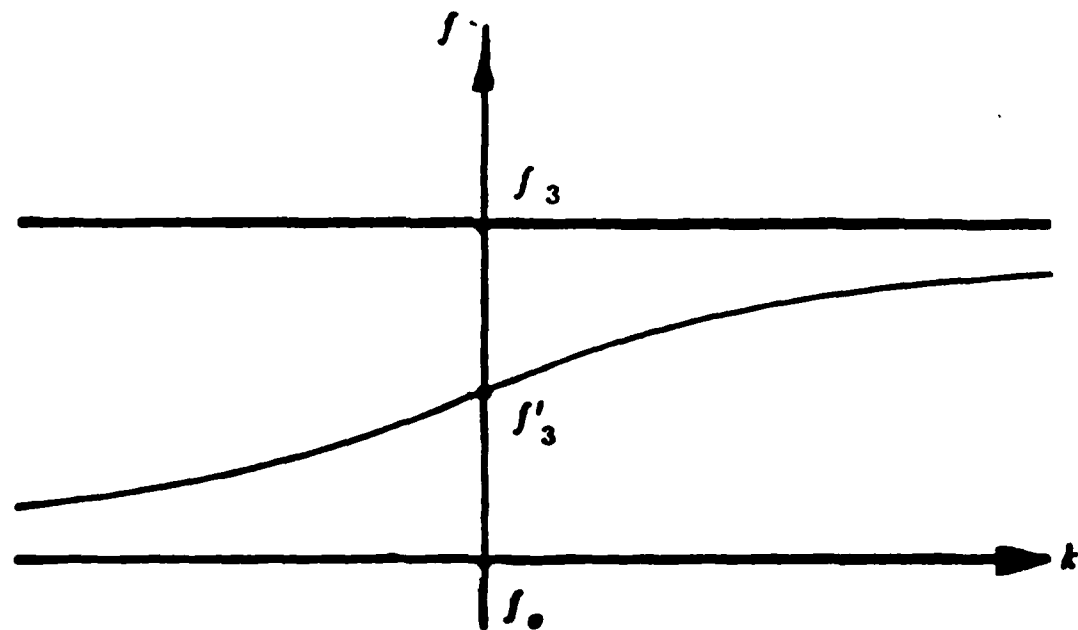


Fig. 5. Qualitative features of the MSVW dispersion diagram for an arbitrary bias-field orientation angle and any one mode

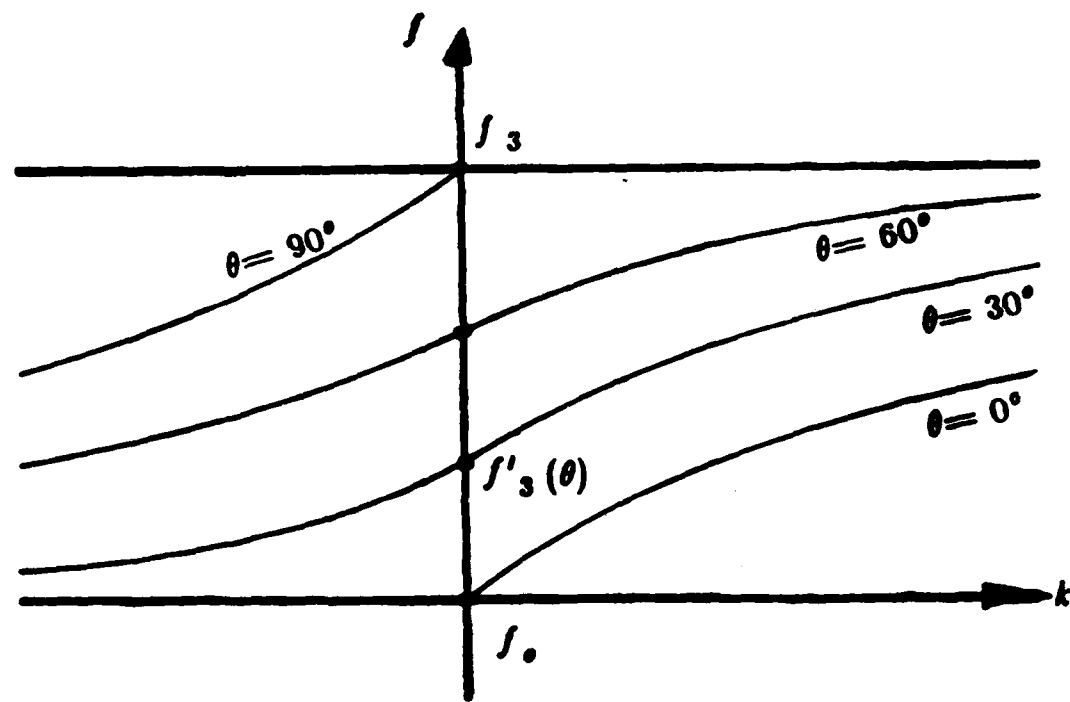


Fig. 6. Effect of changing  $\theta$  on the MSVW dispersion diagram for a given mode.

in watts per unit length along  $y$  by the expression

$$P_{zm} = \int_{-\infty}^{\infty} \mathbf{z}_z \cdot \mathbf{P}_m dz \quad (8)$$

where

$$\mathbf{P}_m = \frac{1}{2} \operatorname{Re}(\mathbf{e}_m \times \mathbf{h}_m^*) \quad (9)$$

is the Poynting vector for the  $m$ th mode. The electric field  $\mathbf{e}_m$  appearing in Eq. (9) is obtained from the Maxwell *curl e* equation, i.e.,

$$\operatorname{curl} \mathbf{e} = -j\omega\mu_s \mathbf{h} \quad (10)$$

The orthogonality properties of the guided MSVW modes may be derived based on a general biorthogonality relation for a guiding structure containing anisotropic materials [4,5]. For the present MSVW modes, this biorthogonality relation translates into the following four relations:

$$\int_{-\infty}^{\infty} (e_{ym}^+ h_{zm}^+ + h_{zm}^+ e_{ym}^+) dz = \omega\mu_s \frac{(1-\mu)}{\mu_s} | k_m | \delta_m^m d \quad (11)$$

$$\int_{-\infty}^{\infty} (e_{ym}^- h_{zm}^- + h_{zm}^- e_{ym}^-) dz = -\omega\mu_s \frac{(1-\mu)}{\mu_s} | k_m | \delta_m^m d \quad (12)$$

$$\int_{-\infty}^{\infty} (e_{ym}^+ h_{zm}^- + h_{zm}^+ e_{ym}^-) dz = 0 \quad (13)$$

$$\int_{-\infty}^{\infty} (e_{ym}^- h_{zm}^+ + h_{zm}^- e_{ym}^+) dz = 0 \quad (14)$$

where

$$\delta_m^m = \begin{cases} 0 & m \neq n \\ 1 & m = n \end{cases} \quad (15)$$

The superscripts + and - represent modal propagation in the positive and negative  $z$

directions, respectively. The notation used to represent subscripts is that a quantity such as  $e_{zm}$  represents the  $z$  component of the vector  $e_m$ , i.e., the electric field associated with the  $m$ th mode.

### 1.2.2. MSVW MODE CONVERSION IN A SINGLE-INTERFACE GEOMETRY

#### 1.2.2.1. PROBLEM FORMULATION

The geometry of the problem treated here is that shown in Fig. 3 where  $z=0$  represents the interface plane and the incident MSVW mode propagates from left to right along the positive  $z$ -axis. In the mode-matching technique, the scattered fields on the two sides of the interface plane are constructed by superimposing all the free modes of the YIG film situated to the respective side of the interface plane. Thus, the total transverse fields in the region  $z < 0$  have the expressions

$$E_y(z, z) = e_{yp}^i + \sum_{n=0}^{\infty} R_{np} e_{yn}^i \quad (16)$$

$$H_z(z, z) = h_{zp}^i + \sum_{n=0}^{\infty} R_{np} h_{zn}^i \quad (17)$$

and in the region  $z > 0$  the expressions

$$E_y'(z, z) = \sum_{i=0}^{\infty} T_{ii} e_{yi}^i \quad (18)$$

$$H_z'(z, z) = \sum_{i=0}^{\infty} T_{ii} h_{zi}^i \quad (19)$$

where the superscripts  $i$ ,  $r$  and  $t$  represent the incident, reflected and transmitted waves, respectively, and the primed and unprimed quantities represent the modal fields in the  $z > 0$  and  $z < 0$  regions, respectively. The incident wave is assumed to be the  $p$ th MSVW mode of the guiding structure in the  $z < 0$  region. The quantities  $R_{np}$  and  $T_{ii}$

are the unknown reflection and transmission amplitude coefficients corresponding to the  $n$ th mode constituent of the reflected and transmitted waves, respectively. The boundary conditions, i.e., continuity of tangential electric and magnetic fields at the interface plane  $z=0$ , yield the infinite set of coupled equations

$$e'_{yp} + \sum_{n=0}^{\infty} R_{np} e'_{yn} = \sum_{n=0}^{\infty} T_{np} e'_{yt} ; z=0 \quad (20)$$

$$h'_{np} + \sum_{n=0}^{\infty} R_{np} h'_{yn} = \sum_{n=0}^{\infty} T_{np} h'_{yt} ; z=0 \quad (21)$$

where the unknown coefficients are found by employing the biorthogonality conditions (11) to (14).

By multiplying Eqs. (20) and (21) by  $(h'_{zm})'$  and  $(e'_{ym})'$ , respectively, integrating the resulting equations with respect to  $z$  over the entire  $z$  axis and then adding these equations one obtains

$$\sum_{n=0}^{\infty} [C]_{ym,zn} R_{np} = - [C]_{ym,yp} \quad (22)$$

where

$$[C]_{ym,zn} = \int_{-\infty}^{\infty} [e'_{yn} h'_{zm} + h'_{zn} e'_{ym}] dz \quad (23)$$

$$[C]_{ym,yp} = \int_{-\infty}^{\infty} [e'_{yp} h'_{zm} + h'_{zp} e'_{ym}] dz \quad (24)$$

The quantity  $[C]_{ym,zn}$  may be considered as the coupling coefficient between the  $n$ th-mode component of the reflected wave and the  $m$ th-mode component of the transmitted wave. Similarly the quantity  $[C]_{ym,yp}$  represents the coupling coefficient of the incident  $p$ th mode to the transmitted  $m$ th mode. Since the index  $m$  runs over an infinite number of integer values, i.e.,  $m=0,1,2,\dots$ , one has an infinite number of simultaneous equations

in an infinite number of unknowns  $R_{np}$ , ( $n=0,1,2,\dots$ ). The solution to these equations may be obtained by truncating the set of equations at a finite number  $N$  so that  $N$  amplitude reflection coefficients  $R_{np}$ ,  $n=0,1,2,\dots,N$ , exhibit a coupling between one another. The corresponding transmission coefficients  $T_{np}$ ,  $n=0,1,2,\dots,N$ , may then be obtained from known  $R'_{np}$ 's by using the relation

$$[\mathbf{U}]_{i'_q, i'_q} T_{np} = \sum_{n=0}^{\infty} [\mathbf{C}]_{i'_q, i'_n} R_{np} + [\mathbf{C}]_{i'_q, i'_p} \quad (25)$$

where

$$[\mathbf{U}]_{i'_q, i'_q} = \int_{-\infty}^{\infty} [e_{yq}^n h_{zq}^n + h_{zq}^n e_{yq}^n] dz \quad (26)$$

The power conservation condition is expressed as

$$P'_{zp} = \sum_{m=0}^{\infty} P'_{zm} + \sum_{q=0}^{\infty} P'_{zq} \quad (27)$$

or

$$\sum_{m=0}^{\infty} R'_{mp} + \sum_{q=0}^{\infty} T'_{mq} = 1 \quad (28)$$

where  $R'_{mp} = \frac{P'_{zm}}{P'_{zp}}$  and  $T'_{mq} = \frac{P'_{zq}}{P'_{zp}}$  are the power reflection and transmission coefficients, respectively, corresponding to a  $p$ th incident mode and  $m$ th free-mode components in the reflected and transmitted waves. The power conservation condition is used to select a proper truncation number  $N$  as well as a pointer to indicate the accuracy of the solution.

### 1.2.2.2. COMPUTED MODE CONVERSION CHARACTERISTICS

While in a rigorous theory one must consider the reflected and transmitted waves

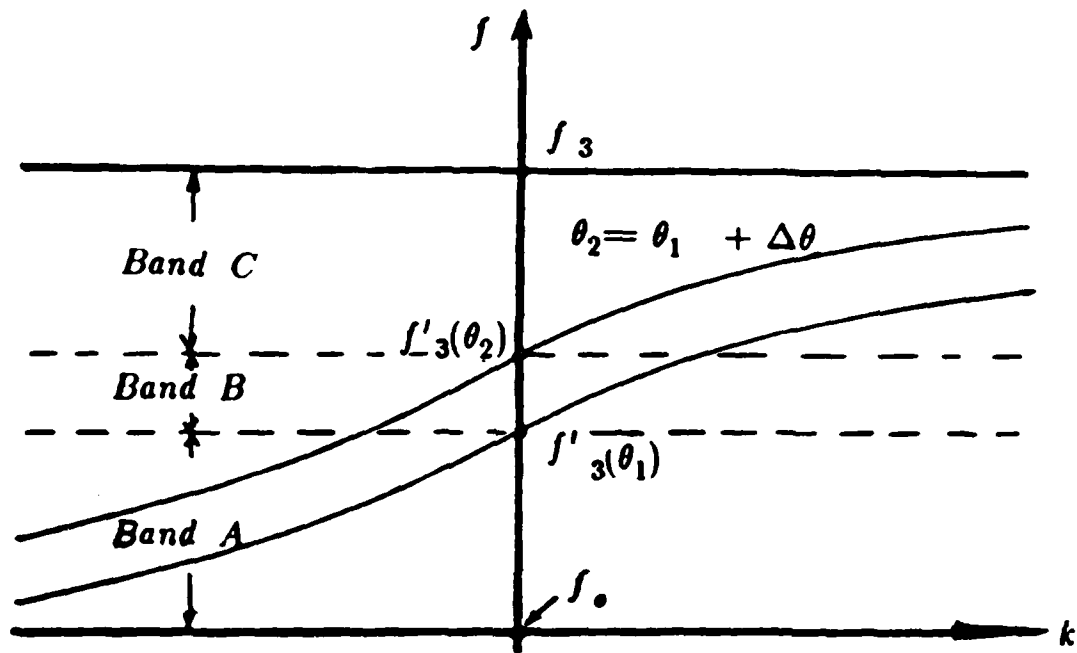


Fig. 7. MSVW dispersion curves for two neighbouring bias-field angles

to be comprised of an infinite number of appropriate free plate modes, in practice one is, of course, interested in mode conversion to a single mode and not to multiple modes. Computations show, in agreement with expectation, that mode conversion to a single mode improves with improvement in phase matching in the direction normal to the YIG film between the incident MSVW and the desired transmitted MSVW mode. This phase-matching condition implies that, the more gradual the discontinuity, the better is the accuracy in using a three-mode-coupling model corresponding to  $N=0$  which assumes a coupling of three modes, viz., the incident wave, one reflected wave and one transmitted wave. The three-mode-coupling computations presented here are for an incident fundamental-mode wave ( $p=0, z < 0$ ), a reflected fundamental-mode wave ( $m=0, z < 0$ ) and a transmitted fundamental-mode wave ( $q=0, z > 0$ ).

Three frequency bands may be qualitatively identified in interpreting the frequency variation of the mode-conversion process. In Fig. 7, MSVW dispersion diagrams are shown for two neighbouring values of  $\theta$ . One immediate observation from this figure is that, while in frequency bands A and C mode conversion will occur between modes of the same type (backward wave-type in band A and forward wave-type in band C), in band B mode conversion will occur between an MSFVW and an MSBVW. Phase-matching is consequently expected to be better in bands A and C than in band B. Thus, one may expect efficient single-mode conversion over a wide band for values of  $\theta$  approaching  $0^\circ$  or  $90^\circ$ . On the other end, one might expect mode matching problems for frequencies lying within band B or for frequencies lying within bands A and C which are close to the resonance frequencies where the divergence in propagation wave number  $k$  becomes large. These predictions are basically borne out by the computations.

Computed frequency variation of the MSVW amplitude reflection  $R$  and transmission  $T$  coefficients is presented in Figs. 8 to 12 for different values of  $\theta_1$  and  $\theta_2$ . These

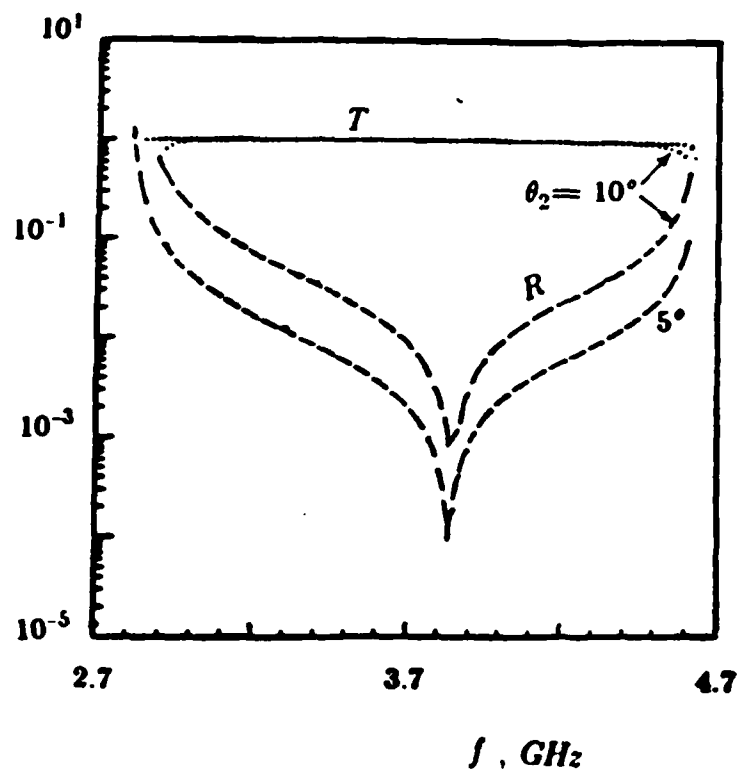


Fig. 8. Frequency variation of reflection R and transmission T coefficients for fixed  $\theta_1$  and two values  $\theta_2=5^\circ$  and  $10^\circ$  of  $\theta_2$

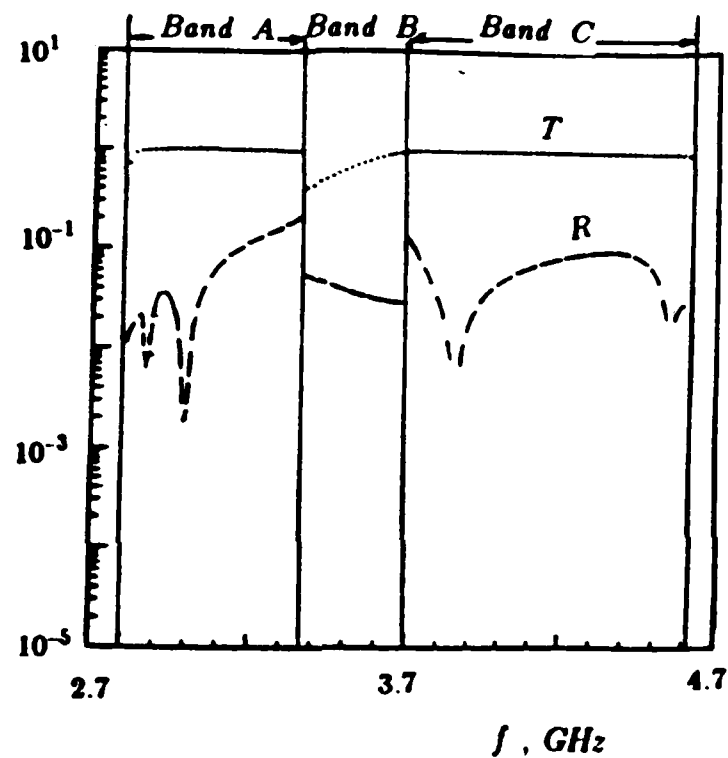


Fig. 9. Frequency variation of R and T for  $\theta_1=30^\circ$  and  $\theta_2=40^\circ$

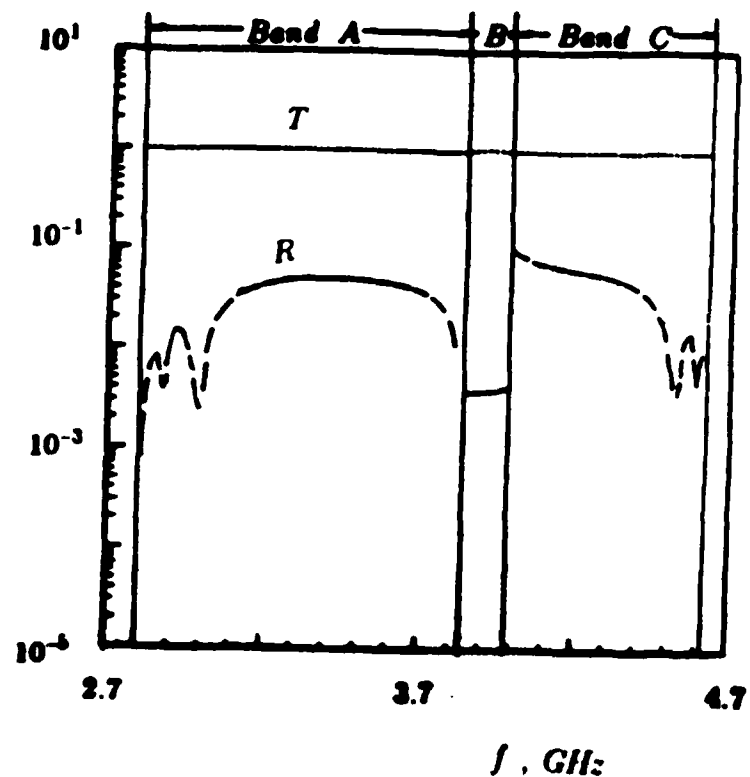


Fig. 10. Frequency variation of R and T for  $\theta_1=45'$  and  $\theta_2=50'$

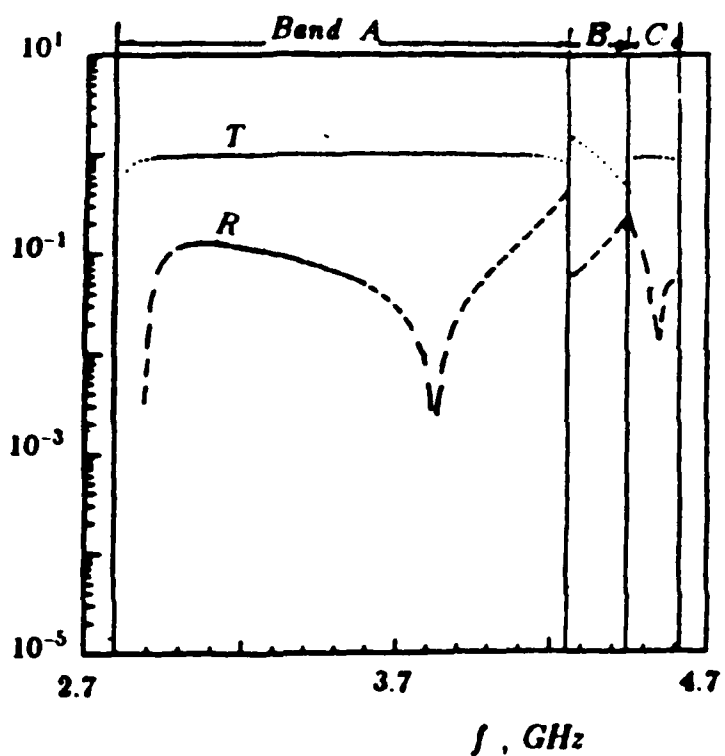


Fig. 11. Frequency variation of  $R$  and  $T$  for  $\theta_1=60^\circ$  and  $\theta_2=70^\circ$

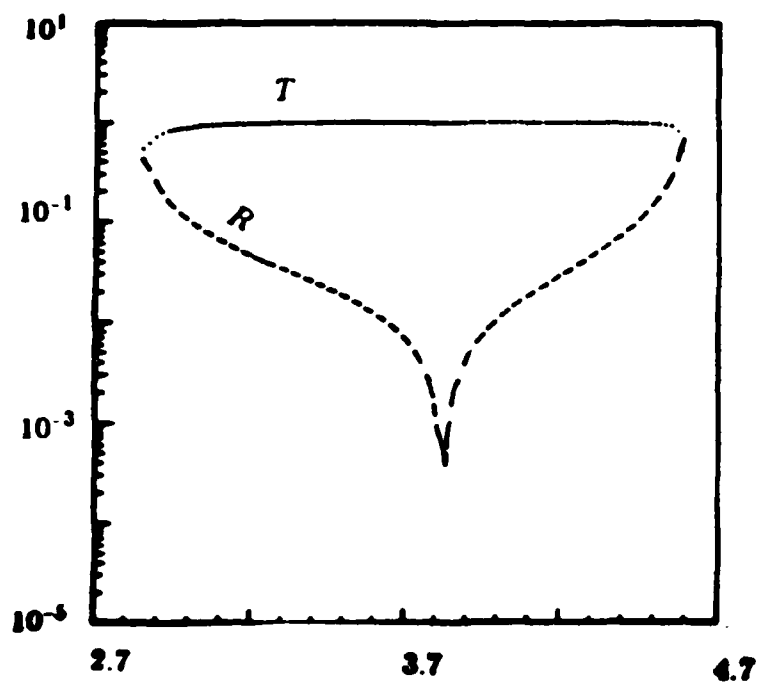


Fig. 12. Frequency variation of R and T for  $\theta_1=80^\circ$  and  $\theta_2=90^\circ$

computations are for a YIG film of thickness  $20\mu m$  and an internal bias field magnitude of  $1 kG$ . In all of these figures, the  $R$  and  $T$  curves are shown by broken and dotted lines, respectively.

In Fig. 8, the incident MSVW is a pure MSVW, i.e.,  $\theta_1=0^\circ$ , and two values of  $\theta_2$  are taken, viz.,  $\theta_2=5^\circ, 10^\circ$ . This figure shows, in agreement with expectation, that  $R$  goes up as the tilt-angle discontinuity is increased. In Figs. 9 to 12, the value of  $\theta_1$  is increased from one figure to the next so that the entire span of values is examined. In these figures, the  $R$  characteristics exhibit a characteristic dip at a frequency of about 3.8 GHz. It is apparent that phase-matching must be good at this frequency. Although it is not obvious why this should happen at about the same frequency for a given magnitude of the internal bias field for all values of  $\theta_1$  and  $\theta_2$ , computations show that changing the magnitude of the internal bias field in either region may relocate the frequency of this dip.

In the figures where, within the  $B$  band, the value of  $T$  exceeds unity, an attempt was made at improving upon the three-mode-coupling model by taking into the coupling formalism additional modes. The computations have not yielded uniform results and it would generally appear that the series expansion technique, i.e., the mode-matching technique, becomes invalid at these frequencies.

The computations of Figs. 8 to 12 are devoid of irregularities present in the corresponding computations of Ref. 3. The latter irregularities manifest themselves in the form of unacceptably large values of  $R$  and  $T$  obtaining at the high and low frequency bounds of the MSVW spectrum and possibly at other frequencies also. It turns out that the difficulties in Ref. 3 arose from the use of orthogonality conditions that are not as accurate as the ones used in this report, i.e. these difficulties are not attributed to a failure of the three-mode-coupling model.

The convergence property of the solutions relative to the number of modes taken into account in the coupling formalism has been explored. Sample results are shown in Tables 1 to 3 where  $M$  represents the number of modes taken into account in the  $z > 0$  region, and only the reflection and transmission coefficients corresponding to conversion into *fundamental* modes are given. The computations for each table are for fixed values of  $\theta_1$  and  $\theta_2$  and three values of  $f$  lying within bands *A*, *B* and *C*. The rate of convergence, in general agreement with expectation, is rapid for medium values of the propagation wave number  $k$  and mode conversion between modes of the same wave-type.

The improvement in mode-matching with increase in the number of modes taken into account in the coupling formalism is also evident in the computations presented in Fig. 13 where modal amplitudes are plotted as a function of mode number for a 20-mode-coupling model. The modal amplitudes, in agreement with expectation, tend toward smaller values as the modal number is increased.

### 1.2.3. MSVW SCATTERING AT A REGION OF GRADUAL BIAS-FIELD DISCONTINUITY

The gradual-bias-field-discontinuity transition region is modeled as a cascade of  $N$  uniform subregions with a total of  $N+1$  interfaces as shown in Fig. 14. In the  $i$ th subregion, which extends over a length  $l_i$ , the bias-field tilt angle has a uniform value of  $\theta_i$  at all points. The total length of the transition region is

$$L = \sum_{i=1}^N l_i$$

#### 1.2.3.1. SCATTERING MATRIX FOR A SINGLE SUB-REGION BASED ON THREE-MODE-COUPLING FORMALISM

The scattering characterization of the  $i$ th sub-region (see Fig. 15) may be cast in terms of three scattering matrices, two of which represent the scattering properties of the boundary planes  $\rho(i)$  and  $\rho(i+1)$  of the sub-region and the third represents the

Table 1 Illustrating the convergence property of scattering solution with the number of modes taken into the coupling formalism.  $M$  stands for the number of reflected modes taken into account which is the same as the number of transmitted modes taken into account. The computations are for  $\theta_1=30^\circ$  and  $\theta_2=40^\circ$ , i.e., band B lies between 3.36 GHz and 3.67 GHz.

$f$	$M$	$ R_{ss} $	$ T_{ss} $	$(P_{refl.} + P_{trans}) / P_{inc}$
3.3 GHz	1	17020	96719	.96442
MSBVW	2	17485	95843	.95500
→	3	17633	.95507	.95081
MSBVW	4	17865	95383	.94935
	5	17692	95365	.94938
	6	17673	95411	.94036
	7	17633	95505	.95211
	8	17573	95643	.95463
3.6 GHz	1	30769	84780	1.0002
MSFVW	2	03536	84717	1.0285
→	3	03786	84667	1.0353
MSBVW	4	03965	84624	1.0376
	5	04112	84585	1.0384
	6	04241	84548	1.0386
	7	04360	84513	1.0384
	8	04474	84478	1.0382
3.9 GHz	1	01943	.99802	.99643
MSFVW	2	02039	99796	.99927
→	3	02097	.99797	1.00063
MSFVW	4	02138	99799	1.00159
	5	02170	99801	1.00233
	6	02197	99803	1.00295
	7	02219	99806	1.00349
	8	02238	99808	1.00396

Table 2 Illustrating the convergence property of scattering solution with the number of modes taken into the coupling formalism. M stands for the number of reflected modes taken into account which is the same as the number of transmitted modes taken into account. The computations are for  $\theta_1=45^\circ$  and  $\theta_2=50^\circ$ , i.e., band B lies between 3.83GHz and 3.99GHz.

<i>f</i>	<i>M</i>	$ R_{ss} $	$(P_{refl} + P_{trans}) / P_{inc}$
3.7 GHz	1	.03682	.99859
MSBVW	3	.03666	.99764
→	4	.03664	.99746
MSBVW	5	.03662	.99734
	6	.03661	.99726
	9	.03659	.99711
	13	.03657	.99700
3.9 GHz	1	.00382	1.09430
MSFVW	3	.00361	1.09530
→	4	.00358	1.09533
MSBVW	5	.00356	1.09530
	6	.00355	1.09531
	9	.00353	1.09532
	13	.00352	1.09530
4.1 GHz	1	.07541	.99483
MSFVW	3	.07102	.99143
→	4	.07092	.99075
MSFVW	5	.07085	.99030
	6	.07070	.98942
	13	.07063	.98901

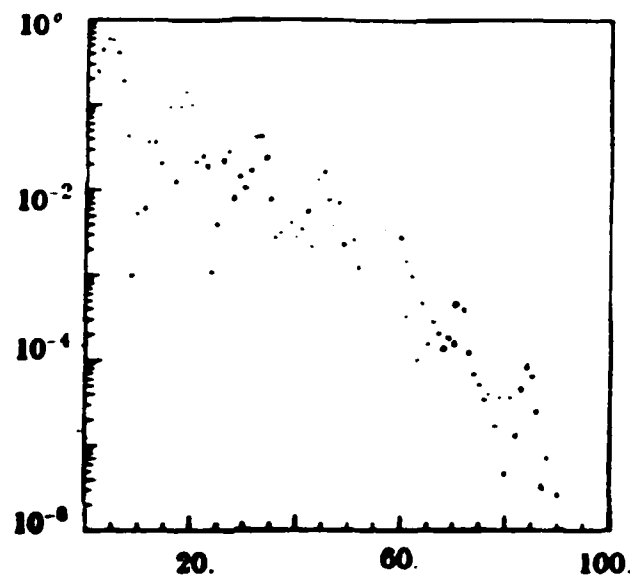


Fig. 13. Modal amplitude reflection coefficients  $R_{ND}$ ,  $N=1$  to 100, plotted as a function of modal index  $N$

property that the length of the sub-region may be treated as a transmission line. The amplitudes of the incident waves at the sub-region are taken to be  $a_i$  and  $a_{i+1}$  and the amplitudes of the reflected waves to be  $b_i$  and  $b_{i+1}$ , with the latter taking into account the mode conversion that occurs between the planes  $p(i)$  and  $p(i+1)$ .

### A. SCATTERING MATRIX FOR A SINGLE INTERFACE

The scattering process at a single interface  $p(n)$  separating two-infinite regions  $n$  and  $m$  is shown in Fig.16. The signal  $a_n$  incident from region  $n$  scatters into a reflected wave  $R_n a_n$  and a transmitted wave  $T_{mn} a_n$ . Similarly the signal  $a_m$  incident at the interface from region  $m$  scatters into a reflected wave  $R_m a_m$  and a transmitted wave  $T_{nm} a_m$ . Thus a total of four waves are involved, i.e., the incident waves  $a_n$  and  $a_m$  and the scattered waves  $b_n$  and  $b_m$ . These four waves are related by the scattering matrix expression

$$\begin{bmatrix} a_{n+1} \\ b_{n+1} \end{bmatrix} = S_{(n)} \begin{bmatrix} a_n \\ b_n \end{bmatrix} \quad (29)$$

where

$$S_{(n)} = \begin{bmatrix} S_{11} & S_{12} \\ S_{21} & S_{22} \end{bmatrix} \quad (30)$$

with

$$S_{11} = - \frac{R_n}{T_{mn}}$$

$$S_{12} = \frac{1}{T_{mn}}$$

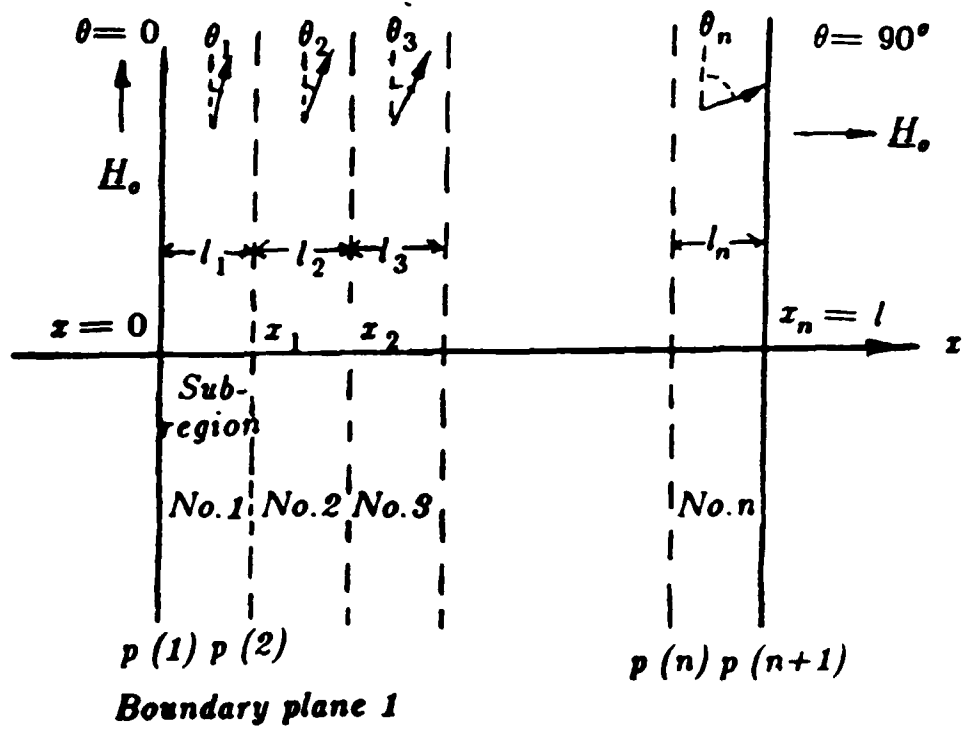


Fig. 14. Geometry of the gradual bias-field-discontinuity transition region modeled as a layered region with fixed bias-field tilt angle in each layer

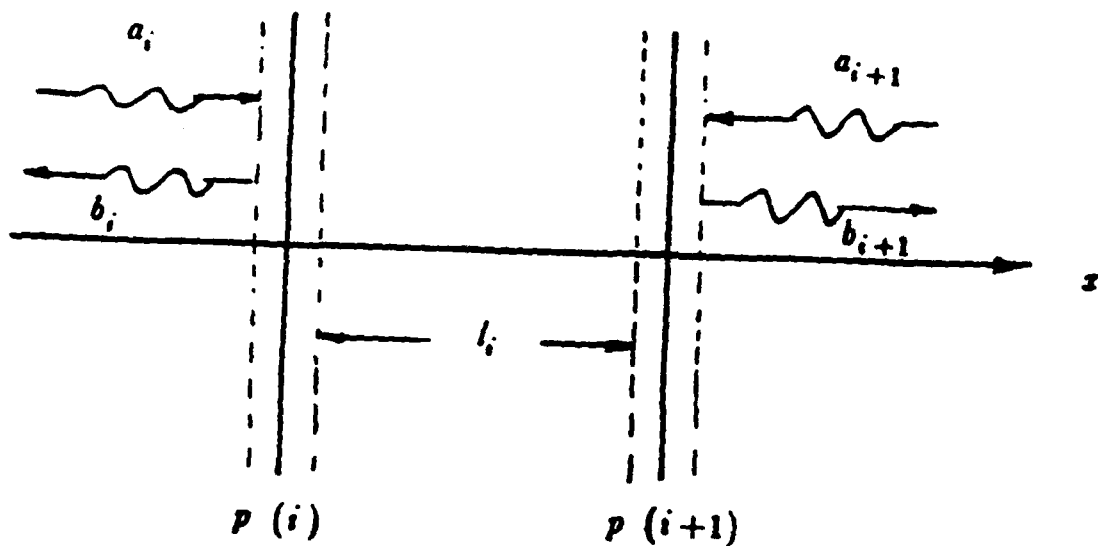


Fig. 15. Scattering model for a single layer or sub-region

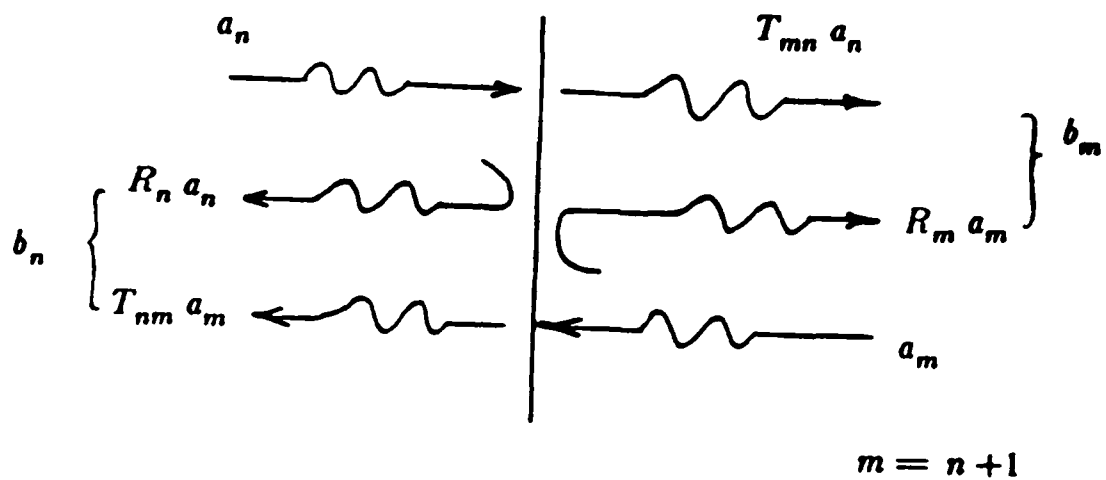


Fig. 16. Scattering model for a single interface constituent of a single layer of Fig. 15

$$S_{21} = T_{nm} - \frac{R_n R_m}{T_{mn}}$$

$$S_{22} = \frac{R_m}{T_{mn}} \quad ; \quad m = n + 1 \quad (31)$$

The subscript  $n$  of the scattering matrix refers to the boundary plane  $p(n)$ . If  $a_m = 0$ , the problem is reduced to the case of three-mode coupling. The reflection and transmission coefficients  $R_n$ ,  $R_m$ ,  $T_{nm}$  and  $T_{mn}$  were obtained in Section 1.2.2. Thus,  $S_{(n)}$  is completely known for any plane  $p(n)$  based on the solution of the three-mode-coupling problem. The general case which also includes higher-order modes has also been treated (see Section 1.2.3.3.).

## B. SCATTERING MATRIX FOR TRANSMISSION LINE

The input and output quantities of a transmission line representing the length  $l_n$  of sub-region  $n$  are shown in Fig. 17. From elementary transmission-line theory these quantities are readily seen to be related by the expression

$$\begin{bmatrix} a_n' \\ b_n' \end{bmatrix} = S_{t(n)} \begin{bmatrix} a_n \\ b_n \end{bmatrix} \quad (32)$$

where

$$S_{t(n)} = \begin{bmatrix} 0 & e^{jk_z l_n} \\ e^{-jk_z l_n} & 0 \end{bmatrix} \quad (33)$$

The quantities  $k_z$  are the wave numbers associated with the waves propagating in the  $\pm z$ -directions.

## C. SCATTERING MATRIX FOR A SINGLE SUB-REGION

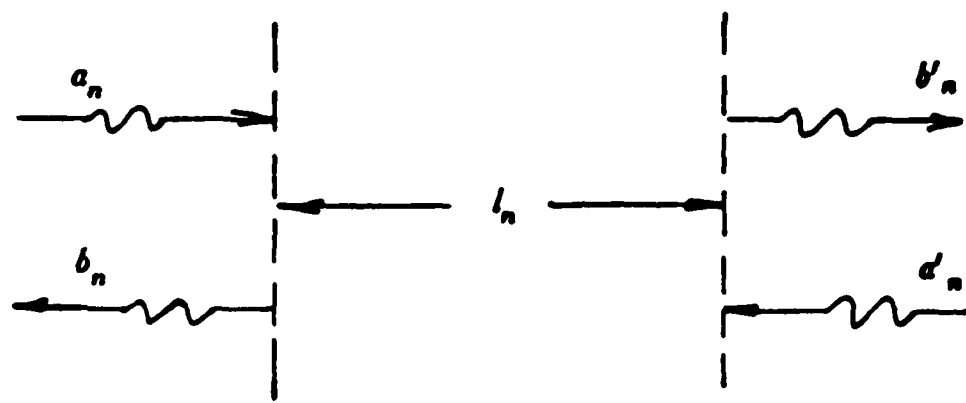


Fig. 17. Scattering parameters for transmission-line portion of the guide section or layer

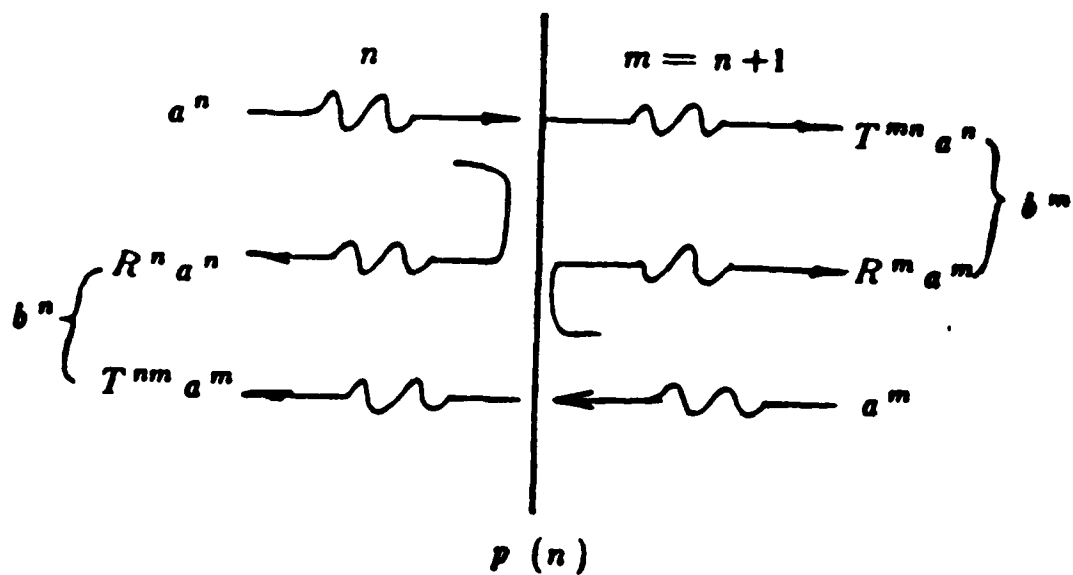


Fig. 18. Generalized scattering process at a single-interface constituent of a single layer or sub-region of Fig. 15

The scattering characterization of a single sub-region is thus given by the cascade relationship

$$\begin{bmatrix} a_{i+1} \\ b_{i+1} \end{bmatrix} = \mathbf{S}_{(i+1)} \mathbf{S}_{l(i)} \mathbf{S}_{(i)} \begin{bmatrix} a_i \\ b_i \end{bmatrix} \quad (34)$$

where  $\mathbf{S}_{(i+1)}$ ,  $\mathbf{S}_{l(i)}$  and  $\mathbf{S}_{(i)}$  are the scattering matrices representing the planes  $p(i+1)$  and  $p(i)$  and the guide length  $l_i$  of the sub-region, respectively.

### 1.2.3.2. SCATTERING-MATRIX FORMALISM FOR THE TRANSITION REGION BASED ON THREE-MODE-COUPLING MODEL

The recognition that the overall transition region represents a cascade of individual sub-regions yields the overall transition-region scattering-matrix relationship

$$\begin{bmatrix} a_{N+1} \\ b_{N+1} \end{bmatrix} = \mathbf{W} \begin{bmatrix} a_1 \\ b_1 \end{bmatrix} \quad (35)$$

where

$$\mathbf{W} = \begin{bmatrix} W_{11} & W_{12} \\ W_{21} & W_{22} \end{bmatrix} = \mathbf{S}_{(N+1)} \mathbf{S}_{l(N)} \mathbf{S}_{(N)} \mathbf{S}_{l(N-1)} \cdots \mathbf{S}_{l(2)} \mathbf{S}_{l(1)} \mathbf{S}_{(1)} \quad (36)$$

In Eq. (35),  $a_1$  is the incident MSFVW amplitude,  $b_1$  is the reflected MSFVW amplitude and  $b_{N+1}$  is the transmitted MSBVW amplitude. If it is assumed that the MSBVW region is a semi-infinite one or matched at the end, then  $a_{N+1}=0$ . The overall transition-region amplitude reflection and transmission coefficients may be related to the components of  $\mathbf{W}$ , i.e.,

$$R = \frac{b_1}{a_1} = - \frac{W_{11}}{W_{12}} \quad (37)$$

$$T = \frac{b_{N+1}}{a_1} = \frac{W_{21}W_{12} - W_{22}W_{11}}{W_{12}} \quad (38)$$

### 1.2.3.3. GENERALIZED MULTI-MODE COUPLING FORMALISM FOR THE TRANSITION REGION

Consider a single-interface plane  $p(n)$  which separates two sub-regions  $n$  and  $m$  where  $m=n+1$  (see Fig. 18). The incoming waves at the interface have amplitudes  $a_n$  and  $a_m$  and the outgoing waves have the amplitudes  $b_n$  and  $b_m$ . These amplitude quantities are now defined by the column matrices

$$\begin{aligned} a^n &= (a_{n0}, a_{n1}, \dots, a_{nN})^T \\ a^m &= (a_{m0}, a_{m1}, \dots, a_{mN})^T \\ b^n &= (b_{n0}, b_{n1}, \dots, b_{nN})^T \\ b^m &= (b_{m0}, b_{m1}, \dots, b_{mN})^T \end{aligned} \quad (39)$$

where the superscript T represents the operation of transpose. Each element in the column matrices has two subscripts, the first one of which denotes the region and the second one the mode number. Thus,  $a_{ni}$  is the  $i$ th incident mode in region  $n$  and  $b_{mj}$  is the  $j$ th outgoing mode in region  $m$ . The  $a$ 's and  $b$ 's are related by the reflection and transmission matrices given by

$$\begin{bmatrix} b^n \\ b^m \end{bmatrix} = \begin{bmatrix} R^n & T^{nm} \\ T^{mn} & R^m \end{bmatrix} \begin{bmatrix} a^n \\ a^m \end{bmatrix} \quad (40)$$

where

$$\begin{aligned}
 R^* &= \begin{bmatrix} R_{00}^* & \cdots & R_{0N}^* \\ \vdots & \ddots & \vdots \\ R_{N0}^* & \cdots & R_{NN}^* \end{bmatrix} \\
 R^m &= \begin{bmatrix} R_{00}^m & \cdots & R_{0N}^m \\ \vdots & \ddots & \vdots \\ R_{N0}^m & \cdots & R_{NN}^m \end{bmatrix} \\
 T^{mn} &= \begin{bmatrix} T_{00}^{mn} & \cdots & T_{0N}^{mn} \\ \vdots & \ddots & \vdots \\ T_{N0}^{mn} & \cdots & T_{NN}^{mn} \end{bmatrix} \\
 T^{nm} &= \begin{bmatrix} T_{00}^{nm} & \cdots & T_{0N}^{nm} \\ \vdots & \ddots & \vdots \\ T_{N0}^{nm} & \cdots & T_{NN}^{nm} \end{bmatrix}
 \end{aligned} \tag{41}$$

The elements of the matrices in Eq. (41) are interpreted as follows.  $R_{ij}^*$  represents the reflection coefficient corresponding to the plane  $p(n)$  which is the ratio of the  $i$ th outgoing mode amplitude to the  $j$ th incident mode, both modes being in the  $n$ th region. Similarly,  $T_{ij}^{mn}$  is the transmission ratio of the  $i$ th outgoing mode on the  $n$  side to the  $j$ th incident mode on the  $m$  side. All these elements are determined in a similar analysis to that in Section 1.2.2. The scattering properties of the interface plane  $p(n)$  are given by the expression

$$\begin{bmatrix} a^m \\ b^m \end{bmatrix} = S^{(n)} \begin{bmatrix} a^n \\ b^n \end{bmatrix} \quad ; \quad m = n + 1 \tag{42}$$

where

$$\mathbf{S}^{(n)} = \begin{bmatrix} -(T^{nn})^{-1}R^* & (T^{nn})^{-1} \\ T^{nn} - R^* (T^{nn})^{-1}R^* & R^* (T^{nn})^{-1} \end{bmatrix} \quad (43)$$

is a  $2(N+1) \times 2(N+1)$  matrix. On each side of an interface plane, a total of  $N+1$  incident and  $N+1$  reflected modes are assumed.

The transmission property of a section of the guide of length  $l_n$  (see Fig. 19) may be represented as

$$\begin{bmatrix} a^n \\ b^n \end{bmatrix} = \mathbf{S}_{t(n)} \begin{bmatrix} a^* \\ b^* \end{bmatrix} \quad (44)$$

where

$$(a^n)^T = (a_{n0}, a_{n1}, \dots, a_{nN})$$

$$(b^n)^T = (b_{n0}, b_{n1}, \dots, b_{nN})$$

$$(a^*)^T = (a_{*0}, a_{*1}, \dots, a_{*N})$$

$$(b^*)^T = (b_{*0}, b_{*1}, \dots, b_{*N})$$

$$\mathbf{S}_{t(n)} = \begin{bmatrix} 0 & \mathbf{D}_- \\ \mathbf{D}_+ & 0 \end{bmatrix}$$

$$\mathbf{D}_+ = \begin{bmatrix} e^{-jk_0^+ l_n} & & & \\ & e^{-jk_1^+ l_n} & & \\ & & \ddots & \\ & & & e^{-jk_N^+ l_n} \end{bmatrix}$$

$$\mathbf{D}_- = \begin{bmatrix} e^{+jk_0^- l_n} & & & \\ & e^{+jk_1^- l_n} & & \\ & & \ddots & \\ & & & e^{+jk_N^- l_n} \end{bmatrix} \quad (45)$$

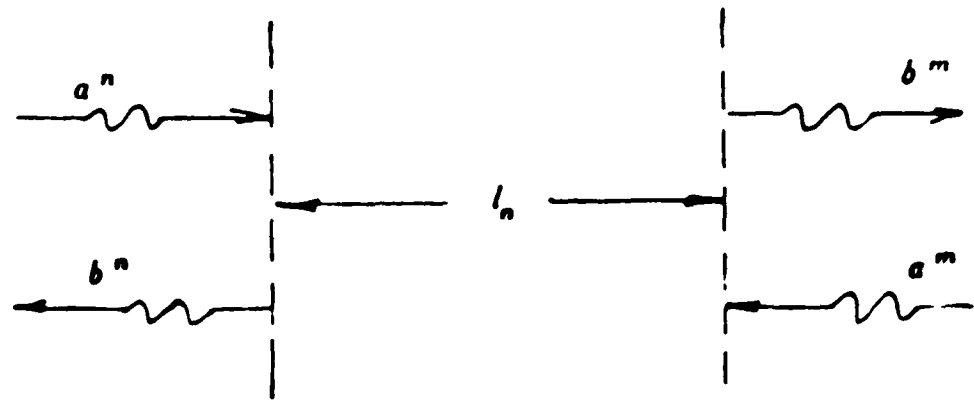


Fig. 19. Generalized scattering model for the transmission-line portion of a layer or sub-region

where  $k_i^+$  and  $k_i^-$  are the wave numbers for the  $i$ th positively propagating and the  $j$ th negatively propagating modes, respectively, in the  $i$ th guide section.

The overall mode conversion property of the entire transition region may be expressed as

$$\begin{bmatrix} a^{N+1} \\ b^{N+1} \end{bmatrix} = \mathbf{W} \begin{bmatrix} a' \\ b' \end{bmatrix} \quad (46)$$

where

$$\mathbf{W} \equiv \begin{bmatrix} W_{0,0} & W_{0,2N+1} \\ \vdots & \vdots \\ \vdots & \vdots \\ W_{2N+1,0} & W_{2N+1,2N+1} \end{bmatrix} = \mathbf{S}_{(N+1)} \mathbf{S}_{(N)}^T \mathbf{S}_{(N)} \mathbf{S}_{(N-1)}^T \cdots \mathbf{S}_{(2)}^T \mathbf{S}_{(1)}^T \mathbf{S}_{(1)} \quad (47)$$

The  $\mathbf{W}$  matrix, which is a  $2(N+1) \times 2(N+1)$  matrix, fully determines the mode conversion properties of the transition region, i.e., the overall transition-region reflection and transmission coefficients can be computed from a knowledge of the incident mode or modes in the pure MSFVW region. Thus, if it is assumed that the incident wave is a single mode which is the fundamental MSFVW mode and the MSBVW region is semi-infinite (or matched), then

$$\begin{bmatrix} a' \\ b' \end{bmatrix}^T = (a_{10}, 0, 0, b_{10}, b_{11}, \dots, b_{1N})$$

$$\begin{bmatrix} a^{N+1} \\ b^{N+1} \end{bmatrix}^T = (0, 0, 0, b_{N+1,0}, b_{N+1,1}, \dots, b_{N+1,N}) \quad (48)$$

where  $a_{10}$  is the amplitude of the fundamental MSFVW mode. The reflection coefficient to the  $i$ th MSFVW mode due to the entire transition line is

$$R_{i,0} = \frac{b_{1i}}{a_{10}}, \quad i = 0, 1, \dots, N \quad (49)$$

The transmission coefficient to the  $j$ th MSBVW mode is

$$T_{j,0} = \frac{b_{N+1,j}}{a_{10}}, \quad j = 0, 1, \dots, N \quad (50)$$

The expressions for  $R_{i,0}$  and  $T_{j,0}$  can be readily put in terms of the elements of the  $W$  matrix. Numerical computations of mode conversion through the transition region may then be performed.

### 1.3. EXPERIMENTAL WORK

The experimental work evolved over three phases. In the first phase, MSW delay-line fabrication techniques were perfected resulting in delay lines with a strong suppression of direct pick-up (typically in excess of 50 dB over most of the 2 GHz to 12 GHz band) and a low insertion loss (typically, without tuning, in the order of 5 dB in the MSSW configuration and 10-15 dB in the MSFVW or MSBVW configuration).

The delay lines employed microstrip transducers defined on Cu-clad Duroid soft substrates which were found to work as well as those on Au-clad alumina hard substrates and are yet much cheaper. YIG-film strips with ends beveled with diamond polishing were used and a high level of ripple suppression in the pass band was achieved, particularly for the case of MSSW's.

In the second experimental phase, a basic experiment on mode conversion was performed. A 3-transducer geometry was employed, with the middle transducer placed half-way between the other two transducers being a diagnostic transducer. The device was first set up as an MSSW delay line and the transmission was measured between the two outer transducers. The device was then physically withdrawn approximately half-way out of the bias field so that a transmitted signal was observed at the center transducer but no signal was observed at the outer receiving transducer. The observed amplitude and phase characteristics of the signal picked up at the center transducer are shown in Fig. 20. Next a horse-shoe magnet was placed over the withdrawn region so that the bias-field orientation in this region was for MSBVW. A signal was now observed at the outer transducer (see Fig. 21). The delay characteristic seen in Fig. 21 corresponds to a BVW and is in qualitative agreement with the overall delay characteristic of a cascade of an MSSW and MSBVW delay lines at the low-frequency end of the overlap frequency band.

For the cascaded geometry comprised of an MSSW delay line followed by a MSBVW delay line, one actually expects, for the case of overlapping passbands, the delay characteristic to initially show a decrease in delay time with increasing frequency and then an increasing delay time with further increase in frequency. The observed delay characteristic in the monolithic structure exhibits a basically monotonic decrease in delay time with increasing frequency, a feature that is at variance with expectation at the high frequency end of the passband spectrum. It was concluded that, while the observed signal in Fig. 21 might represent mode conversion, this was not necessarily fully proved.

The difficulties in the experiment lie mainly in the implementation of a controlled slowly varying bias field in the transition region as well as the inevitably strong interac-

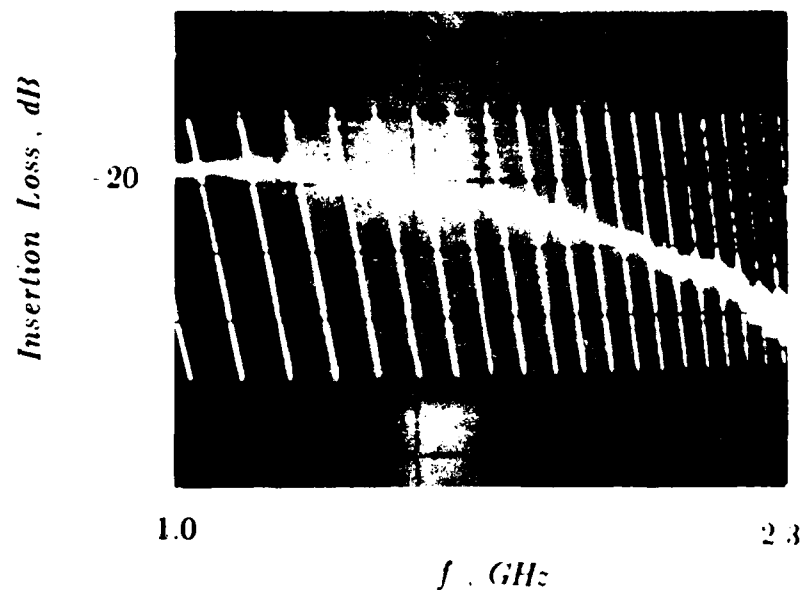


Fig. 20. Amplitude and phase characteristics observed at the center transducer when only the MSSW bias field is present and the delay line is withdrawn half-way out of the magnet poles.

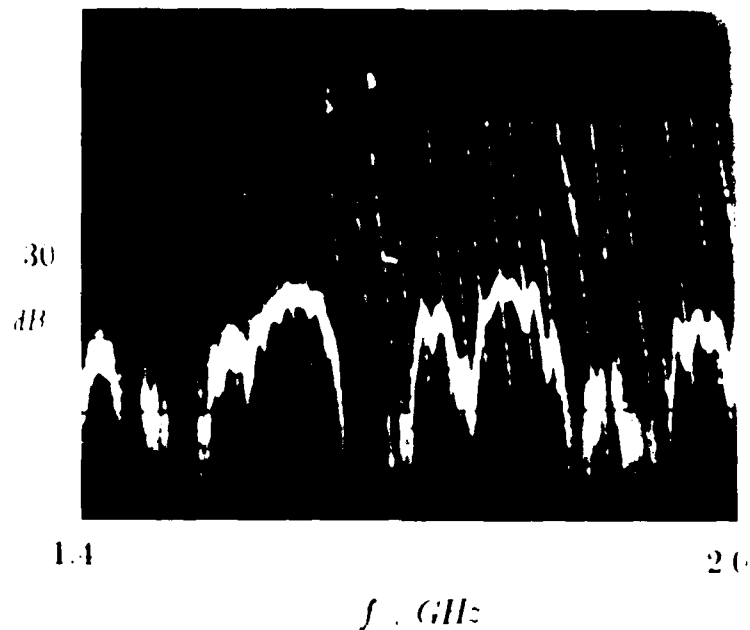


Fig. 21. Observed signal at the outer receiving transducer obtained when the horse-shoe MSBVW bias field is imposed on the withdrawn half of the delay line



Fig. 22. Photograph of 3-transducer delay-line device in which the center transducer can be moved with a screw arrangement.



Fig. 23. Photograph showing added magnetic circuit screwed to the electromagnet poles.

tion between the magnet systems because of their close proximity. Furthermore, the size of the poles of the horse-shoe magnet is quite significant compared to the dimensions of the YIG film. Thus, while it seemed like a good first try to withdraw the YIG film half-way out of an MSSW bias field and then impose the field of a horse-shoe magnet, the need for a careful design of a precision *single* magnetic circuit was fully recognized.

In order to perform a more careful study of the mode-conversion phenomenon in the above experiment, a three-transducer delay-line device was constructed which permitted the position of the center diagnostic transducer to be variable over most of the length of the YIG film. A photograph of this device is shown in Fig. 22. An important diagnostic study that was attempted *albeit* without success is that of measuring the physical lengths of the forward and backward-wave regions as well as the length of the transition region. The difficulty in performing this study arose from the sensitivity of the two interacting magnet systems to any slight movement of either magnet system. One would draw the conclusion, as a result of the second phase of the experimental study, that, while MSW transmission in a delay line subjected to two biasing magnetic systems (one intended to produce an MSSW bias-field orientation in the first half of the delay line and the other intended to produce an MSBVW bias-field orientation in the second half of the delay line) was observed, it was not conclusive that *unambiguous* mode conversion had indeed been observed.

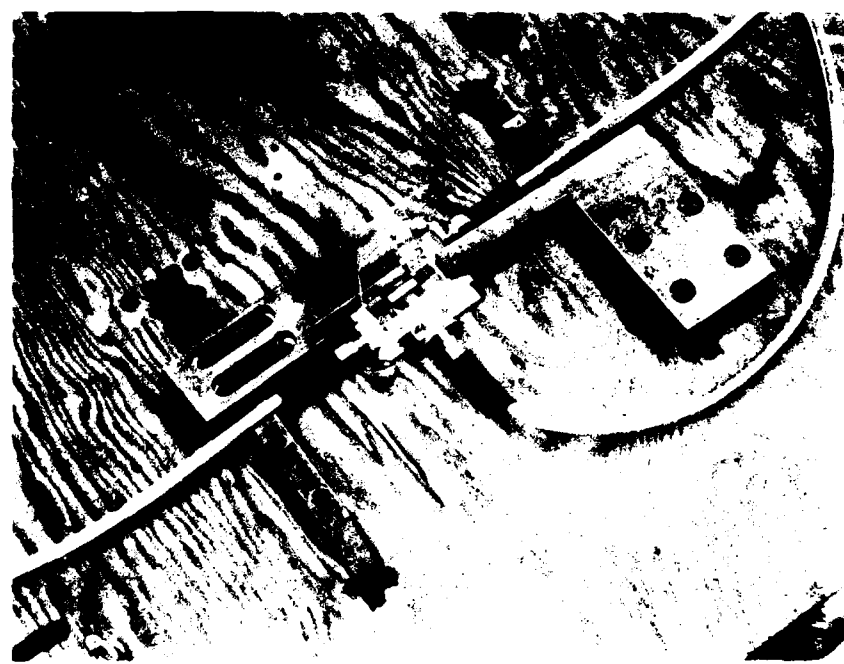
The third phase of the experimental study was concerned with the design and implementation of a precision magnetic circuit which was machined out of steel and screwed on to the electromagnet poles. While such a precision magnet design was awaited, an empirical design was machined and attached to the poles of the electromagnet. A photograph of this empirical design is shown in Fig. 23. A photograph of the new magnet poles with the three-transducer delay device placed within them is shown in

Fig. 24. The bias-field orientation profile was tested using iron filings and was qualitatively of the type desired. A tuning of the orientation or magnitude of the bias field was achieved with the use of coils placed around the poles. Experimental observations were made which were inconclusive. However, before further work could be carried out, new theoretical understanding into the mode-conversion process was attained which indicated a serious problem in the achievement of mode conversion (see section 1.4) and led to a termination of the general effort.

An alternative approach to the problem of observing mode conversion had also been initiated which involved the use of a curved YIG-film strip, e.g., a right-angle bend. The main attraction of using a curved YIG-film strip is that it should afford a much better control over the bias fields separating the two wave-type regions. A central question attaching to the practicality of using a YIG-film bend whether the propagation loss in going around the bend is tolerable. The phosphoric-acid process for etching out a curved YIG-film strip has been well established in our laboratory but the theoretical difficulties explained in Section 1.4 also forced a termination of this effort.

#### 1.4. NEW THEORETICAL DEVELOPMENTS

Computations of mode conversion in a *single-interface* geometry with slightly differing bias fields on either side of the interface have shown efficient mode conversion over a wide band (see Section 1.2.2.). However, attempts at calculating the mode-conversion characteristics for the case of a *gradual bias-field-discontinuity* transition region ran into snags which were tracked down to the  $k=0$  point on the MSVW dispersion diagram (see Fig. 6) occurring at a unique value of  $\theta$  for a fixed frequency. The  $k=0$  point represents a cut-off condition: A lower cutoff frequency exists even when the electromagnetic retardation effect is taken into account (see Attachment C). At the



**Fig. 24. Photograph of added magnet poles with the 3-transducer delay-line device placed within them.**

point along the guide where cut-off obtains propagation along the guide simply ceases to exist. In other words, the sub-region of the transition region where the bias-field tilt angle  $\theta$  for the *chosen* frequency yields the MSW wave number  $k=0$  simply prevents the signal from going through it. It follows that mode conversion from MSFVW to MSBVW in going through a gradual bias-field-discontinuity transition region is theoretically not possible. This catastrophic condition has been investigated in considerable detail in an attempt at finding possible means of overcoming the cut-off condition but this effort has been unsuccessful.

### 1.5. CONCLUSIONS

A theoretical formalism for handling the problem of MSVW mode conversion across a region of bias-field discontinuity was successfully completed employing the mode-matching technique. Computations of mode conversion across a plane of small discontinuous change in bias-field orientation indicate efficient mode conversion over a wide bandwidth. Attempts at computing the mode-conversion properties of a gradual-bias-field-discontinuity region ran into a snag which was tracked down to the existence of the  $k=0$  point on the MSVW dispersion diagram. For any value of the signal frequency within the MSVW passband, there exists a unique angle lying between  $0^\circ$  and  $90^\circ$  which yields  $k=0$  for the MSVW wave number. The  $k=0$  point represents a catastrophic condition since it implies that MSVW propagation and, therefore, conversion would not occur across the sub-region of the transition region where  $k=0$ . This catastrophic discovery rendered further work on MSVW mode conversion across a region of bias-field discontinuity without merit and thus forced a termination of the effort.

## CHAPTER 2

### DISPERSION OF A TIME-LIMITED MSFVW CW PULSE

#### 2.1. INTRODUCTION

MSW's are pronouncedly dispersive in geometries devoid of dispersion-control features. The present chapter reports the main results of a detailed theoretical and experimental study of the dispersion of a time-limited MSFVW CW pulse. The theory has incorporated the frequency response of the input and output microstrip transducers in a delay-line geometry and has yielded results that are in excellent agreement with the experimentally observed oscilloscope pictures of delayed pulses picked up by an output microstrip transducer whose spacing from the input transducer is made variable through the placement of the output transducer on a platform movable with a screw arrangement (see Fig. 1.22).

The theoretical computations, if performed by a brute-force method, would be based on the standard Fourier transform technique. Thus, by representing a time-limited CW pulse in terms of its Fourier spectrum, one simply finds the change in the amplitude (if losses are included) and the phase of every single frequency component of the signal, and then at the end of the propagation the individual frequency components are combined to synthesize the delayed pulse signal.

Difficulties in the inverse transform process arise whenever the integrand of the transformation is an ill-behaved function, e.g., a rapidly oscillating function which is very much the case with MSW pulses. An elegant approach to overcoming this problem is provided by the fast Fourier transform (FFT) technique which assumes that, instead of a solitary or single pulse, there exists a train of pulses that are periodic in time. The existence of a train of pulses sufficiently separated in time is incidentally always the case in experiments.

The FFT technique, with its attendant process of summing over weighted discrete Fourier components, makes the computational process extremely efficient, i.e., the computational time is significantly shorter because of fewer computational points required than in the brute-force or direct method of performing the integration represented by the inverse Fourier transform. The degradation of the accuracy in the computations goes up as the number of computational points per temporal cycle goes down. This degradation of envelope distortion is not large with the FFT technique even when only one computational point per carrier cycle is employed. The FFT technique also allows propagation loss to be included in the calculation since complex quantities are an intrinsic part of the FFT approach. A detailed theory of the FFT technique as well as its implementation, described in a 1985 doctoral thesis at Stony Brook [6], is not presented here.

## 2.2. BASIC THEORY OF PULSE DISPERSION

Let the CW pulse be defined by the function

$$\phi(x=0, t) = A \Pi\left(\frac{t}{\tau}\right) \cos 2\pi f_c t \quad (1)$$

at its starting point  $x=0$  where  $A$  is the pulse amplitude,  $f_c$  is the carrier frequency and  $\Pi\left(\frac{t}{\tau}\right)$  is the window function

$$\Pi\left(\frac{t}{\tau}\right) = \begin{cases} 1, & |t| \leq \tau/2 \\ 0, & |t| \geq \tau/2 \end{cases} \quad (2)$$

(Strictly, a *precisely* rectangular MSFVW *input* pulse is not possible because of the finite bandwidth over which MSFVW's exist).

Since the function  $\phi(x=0, t)$  is symmetric in time and extends only over the time period  $|t| \leq \tau/2$ , the Fourier transform

$$\Phi(x=0, f) = \int_{-\infty}^{\infty} \phi(x=0, t) \exp(-j 2\pi f t) dt \quad (3)$$

of  $\phi(x=0, t)$  may be written as

$$\Phi(x=0, f) = \frac{A \tau}{2} [\text{sinc } (f - f_c) \tau + \text{sinc } (f + f_c) \tau] \quad (4)$$

Since MSFVWs exist only in the band  $f_s < f < f_s$ , only positive frequencies are allowed in Eq. (4), i.e.,

$$\Phi(x=0, f) = \frac{A \tau}{2} \text{sinc } (f - f_c) \tau \quad (5)$$

The foregoing signal  $\phi(x=0, t)$  was at the point  $x=0$ . As time increases, the pulse will move so that at any point  $x > 0$ ,

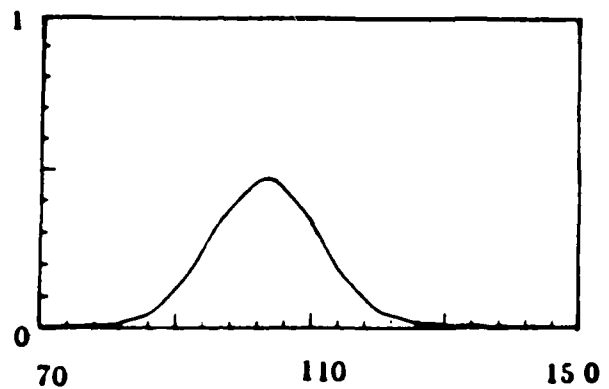
$$\Phi(x, f) = \Phi(x=0, f) \exp(-jkx) \quad (6)$$

The inverse Fourier transform of Eq. (6) reconstitutes the pulse in space and time, yielding

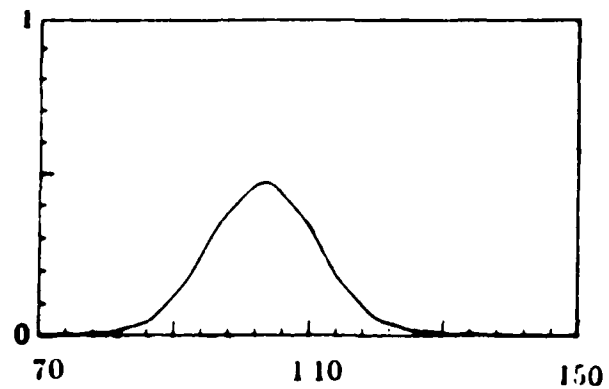
$$\phi(x, t) = A \tau \int_{f_s}^{f_s} \frac{\sin \pi(f - f_c) \tau}{(f - f_c) \tau} \cos(2\pi f t - kx) df \quad (7)$$

### 2.3. NUMERICAL RESULTS

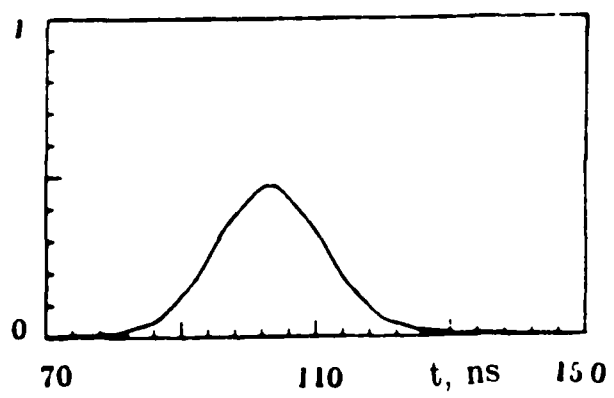
The computational efficiency of the FFT technique vis-a-vis the direct or brute-force integration technique in the computation of pulse distortion is demonstrated in the computations of Figs. 1 and 2. The FFT computations are given in Fig. 1 while the direct integration results are given in Fig. 2. These figures represent the shape of a 20 ns pulse of rf frequency  $f_c = 4$  GHz after propagation through a distance of 1 cm. Three sets of computations are presented in each of these figures corresponding to 2, 4 and 8 computed points per carrier cycle, respectively. The shape of the pulse envelope in Fig. 1 remains essentially unchanged as the number of computed points per cycle is reduced from 8 to 2. On the other hand, the computations employing the direct integration approach (which computes the carrier signal rather than the envelope) show a significant degradation of the envelope as the number of computed points per rf cycle is reduced.



(a)



(b)



(c)

Fig. 1. FFT-computed envelope of a 20 ns MSFVW pulse of rf frequency  $f_c = 4$  GHz after a propagation pathlength of 1cm for three different values of computed points  $N_c$  per rf cycle: (a)  $N_c = 2$ , (b)  $N_c = 4$ , (c)  $N_c = 8$ .

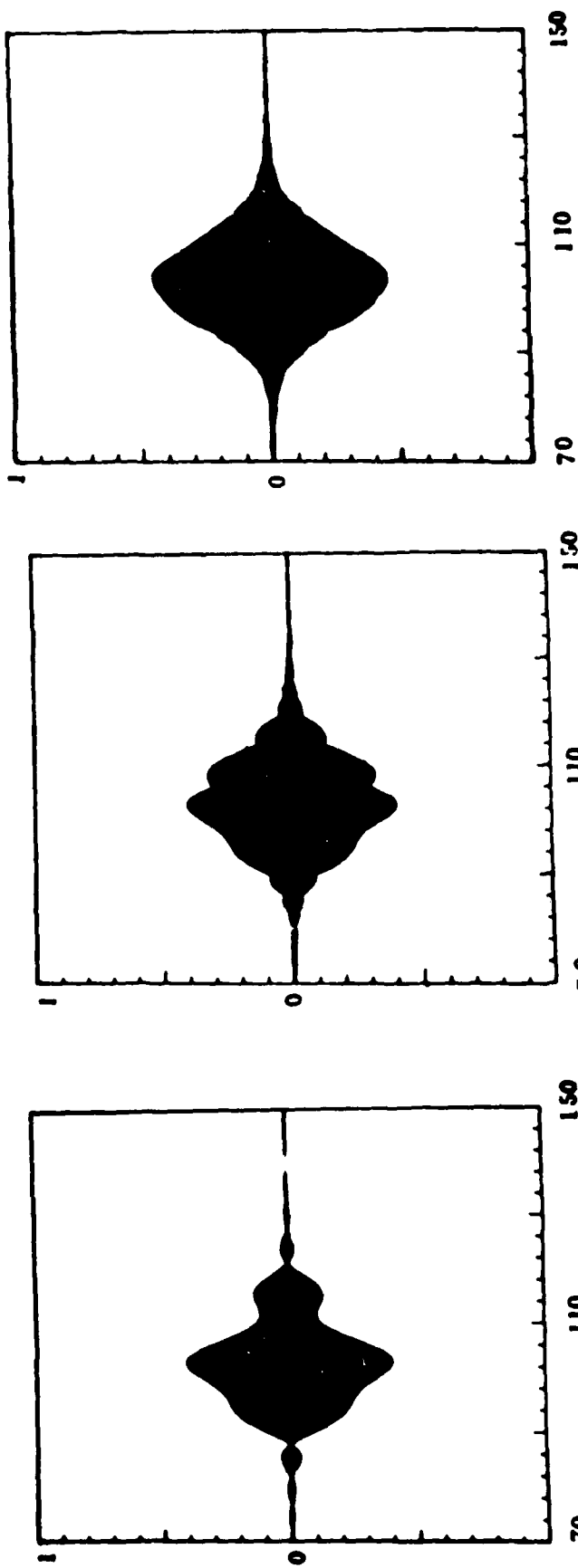


Fig. 2. Computed carrier signal of the MSFVW pulse of Fig. 1 using the direct integration approach for the same number of values of computed points  $N_c$  per rf cycle: (a)  $N_c = 2$ , (b)  $N_c = 4$ , (c)  $N_c = 8$ .

In Fig. 3, the spreading of the envelope of a pulse of width 20 ns at  $x=0$  is shown for different positions  $x$  of the observation point, i.e.,  $x=0.5$  cm, 0.75 cm, 1.00 cm and 1.25 cm. As expected, the distortion occurs primarily in the form of stretching of the pulse width and the attendant "peaking" of the pulse.

A significantly smaller level of envelope distortion achievable in a *nondispersive* geometry is demonstrated in the computations of Fig. 4 which are for a nondispersive double-YIG-film-layered structure. In the computations, the upper YIG film has a thickness of 65  $\mu\text{m}$  and saturation magnetization of 2kG, the lower film has a thickness of 10  $\mu\text{m}$  and saturation magnetization of 1.75 kG, and a ground plane is placed at a distance of 100  $\mu\text{m}$  above the top YIG film. The overshoot at the skirts of the pulse envelope is the unavoidable result of the finite bandwidth over which MSFVWs exist.

#### 2.4. EXPERIMENTAL RESULTS

The experimental work on the dispersion of an MSFVW pulse was carried out using a 41  $\mu\text{m}$  thick YIG film with a saturation magnetization of about 1.5kG. The delay line measurements made at rf frequencies  $f_c = 2.06$  GHZ and  $f_c = 2.16$  GHz are shown in Figs. 5 and 6, respectively. These measurements were made directly on the Tektronix 7104 oscilloscope without the use of a crystal detector. It is evident that, except for spurious signals following the main delayed pulse, the agreement between experiment and theory is generally excellent.

#### 2.5. CONCLUSION

The results of a theoretical and experimental study of MSFVW pulse distortion with propagation are reported. It is demonstrated that the FFT technique of computation of the distortion in pulse envelope with propagation is significantly more efficient

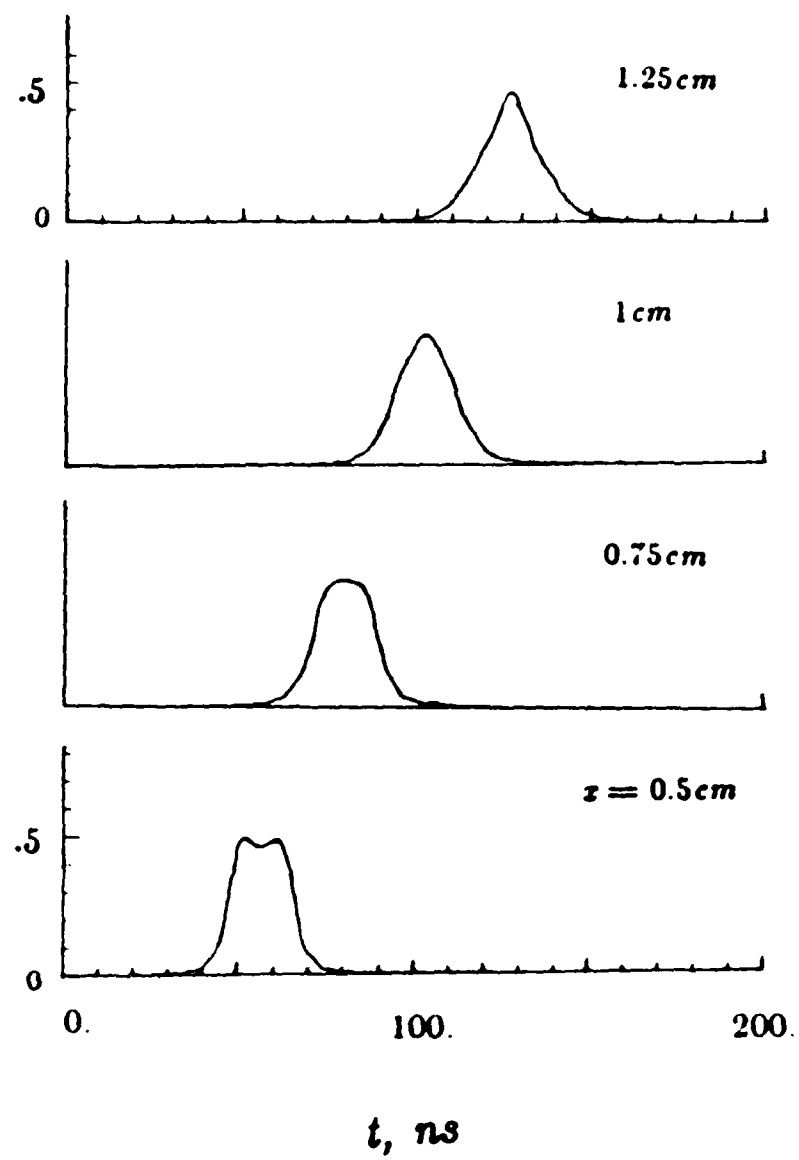


Fig. 3. Computed envelope of a 20 ns MSFVW pulse for different distances  $x$  of propagation

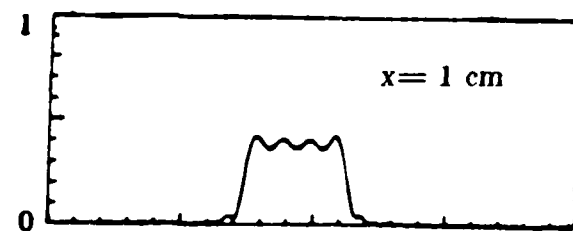
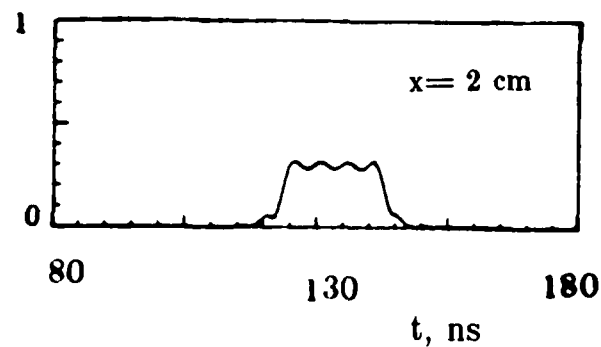


Fig. 4. Computed envelope of a 20 ns MSFVW pulse for  $x=1 \text{ cm}$  and  $x=2 \text{ cm}$  propagation path-lengths in a *nondispersive* double-YIG-film-layered structure.

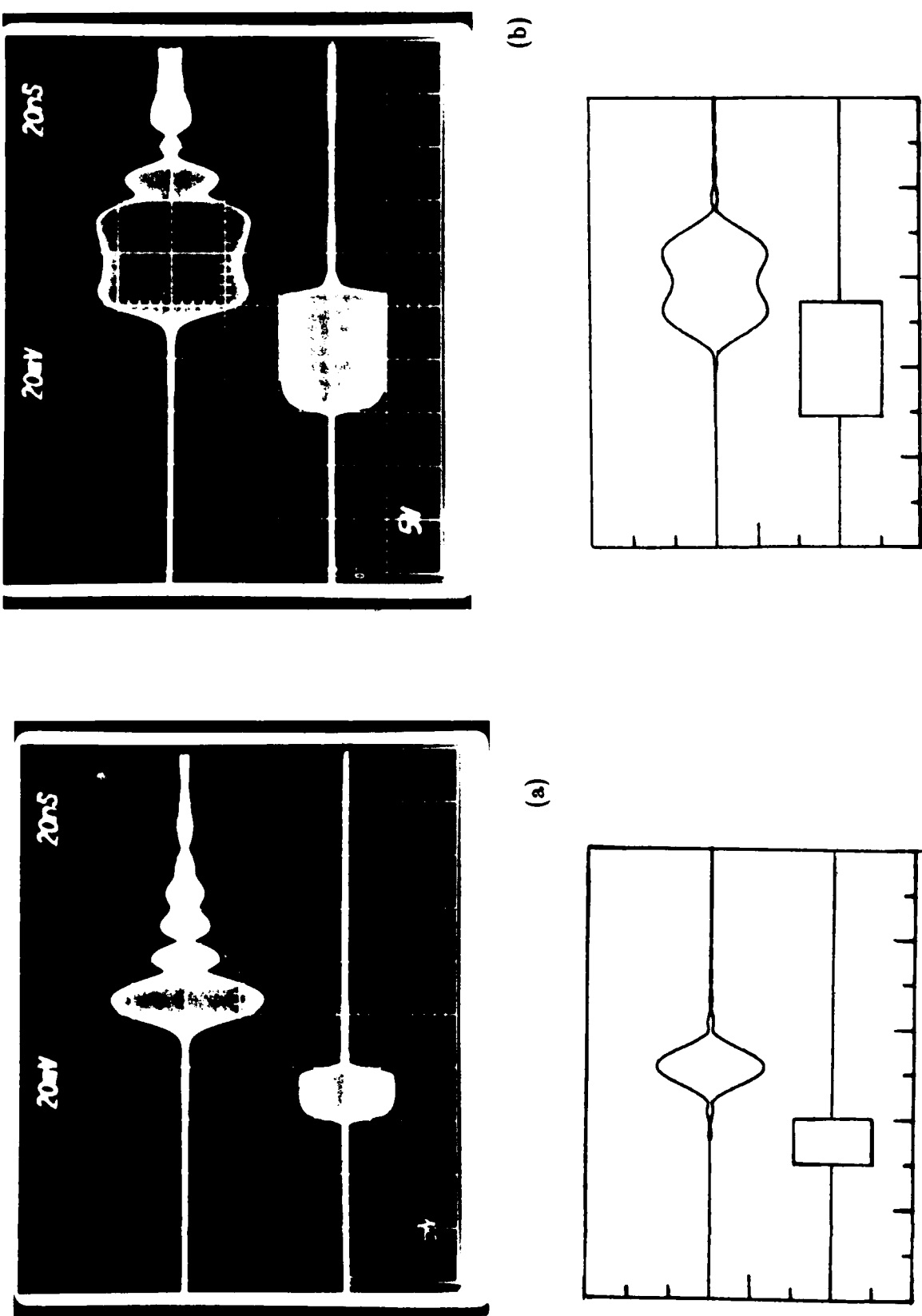


Fig. 5. Experimental (top figure) and theoretical (bottom figure) MSFVW delay line results of a  $f_s = 2.06$  GHz pulse at  $x = 0.6$  cm for two values of starting pulse width: (a) 20 ns, (b) 50 ns

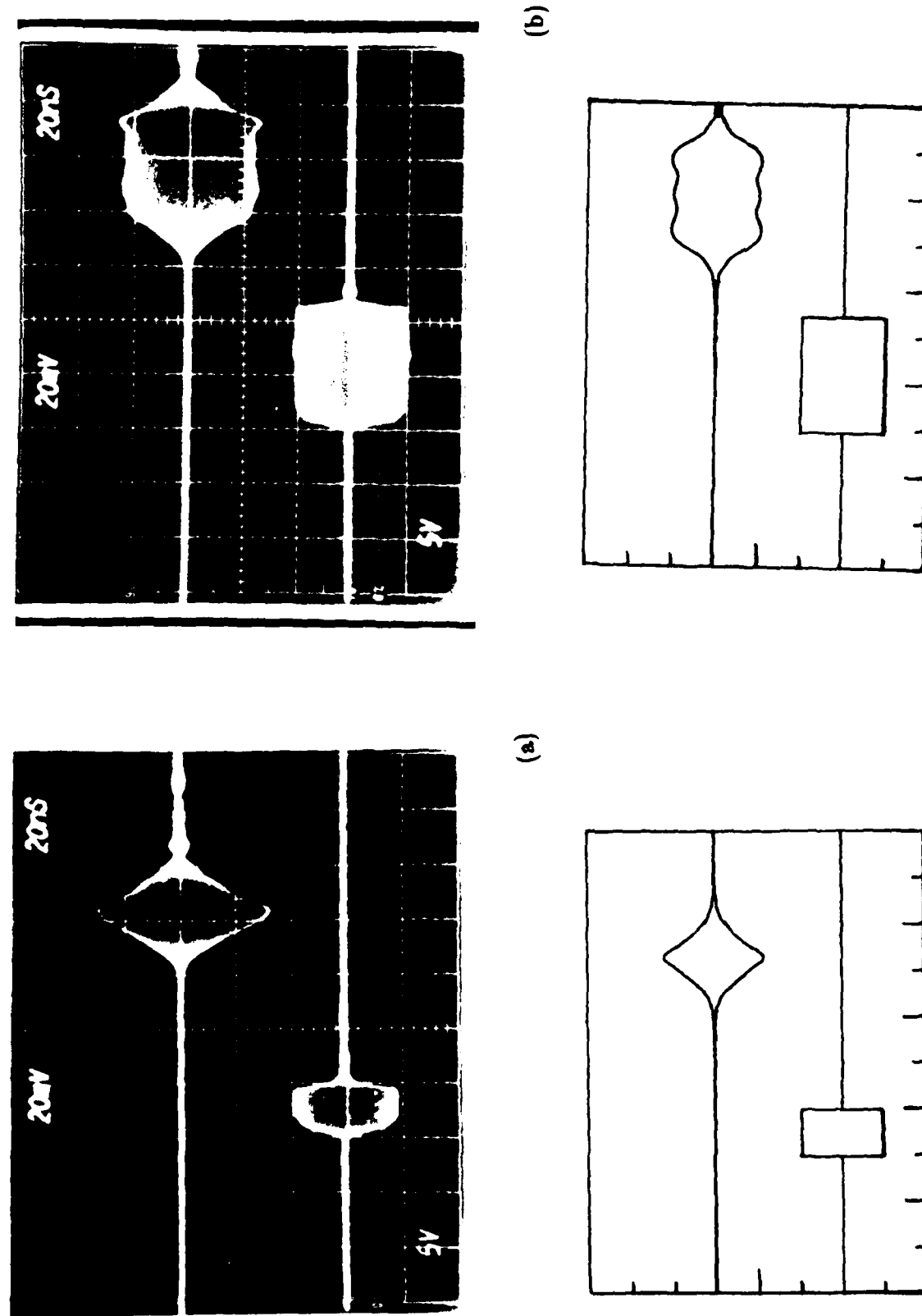


Fig. 6. Same as Fig. 5 except for  $f_c = 2.16$  GHz and  $x = 1.2$  cm.

than the direct or brute-force integration technique. The agreement between experiment and theory on the shape of the delayed pulse is generally excellent.

## REFERENCES

1. J.C. Sethares, J.M. Owens and C.V. Smith, Jr., "MSW nondispersive, electronically tunable time delay elements," *Electronics Letters*, **16**, 825 (1980)
2. J.P. Parekh and K.W. Chang, "Nondispersive MSFVW propagation in a triple-YIG-film-layered structure," in *Proc. IEEE*
3. H.S. Tuan, J.P. Parekh and K.W. Chang, "Magnetostatic-volume-wave mode conversion at a region of bias-field discontinuity," in *Proceedings of the 1983 IEEE Ultrasonics Symposium*
4. A.D. Bresler, G.H. Joshi and N. Marcuvitz, "Orthogonality properties for modes in passive and active uniform wave guides," *J. Appl. Phys.* **29**, 794 (1958)
5. L.R. Walker, "Orthogonality relation for gyrotropic wave guides," *J. Appl. Phys.* **28**, 377 (1957)
6. K.W. Chang, "Study of magnetostatic-wave constant delay lines and convolvers," Ph.D. (EE) dissertation, State University of New York at Stony Brook (1985)

## ATTACHMENT A

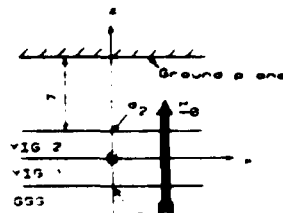


Fig. 1. Geometry of the problem.

### Nondispersive Magnetostatic-Forward-Volume-Wave Propagation in a Double-Layered YIG-Film Structure

J. P. PAREKH AND K. W. CHANG

**Abstract**—Computed group-delay characteristics are presented illustrating the significant improvement in bandwidth for nondispersive magnetostatic-forward-volume-wave propagation that may be achieved utilizing a double-YIG-film-layered structure over a single-YIG-film geometry.

A theoretical prediction, reported briefly elsewhere [1], that a significant improvement in bandwidth for nondispersive magnetostatic-forward-volume-wave (MSFVW) propagation over the single-YIG-film/dielectric/ground-plane configuration may be achieved using a double-YIG-film-layered structure in conjunction with a separated ground plane is described here for saturation magnetization parameters that are readily realizable in practice. The computed delay versus frequency characteristics presented here furthermore show that the requirement for the achievement of bandwidth improvement stated in [1], i.e., the YIG film closer to the ground plane possess the higher saturation magnetization of the two films, may in fact be relaxed so as to permit either film to possess the higher saturation magnetization.

The geometry of the problem under consideration is shown in Fig. 1. The YIG film of thickness  $d_1$  grown on the GGG substrate (YIG-1 film) is overlaid with a different YIG film of thickness  $d_2$  (YIG-2 film). A perfect electrical ground plane is placed at a height  $h$  above the top film surface. (Although a practical ground plane would give rise to conductive loss, the computations show that optimum MSFVW nondispersive characteristics are obtained if the ground plane is sufficiently separated from the top YIG-film surface (typically by 100  $\mu\text{m}$  or more) so that the conductive loss is rendered insignificant (in the order of 1 dB/cm or less)). An external saturating bias field  $H_0 = H_0 z_0$  applied normal to the films produces internal fields  $H_{11} = H_0 - M_{01} z_0$  and  $H_{22} = H_0 - M_{02} z_0$  in the two films where  $M_{01}$  and  $M_{02}$  are the values of the saturation magnetization for the respective films. For straight-crested MSFVW propagation along  $x$ , with  $x$  and  $t$  variation  $\exp(i(2\pi f t - kx))$ , the dispersion relation is [1]

$$(\mu_2 + \mu_1 \tanh kh) \tan \beta_1 k d_1 \tan \beta_2 k d_2 + \beta_1 (\mu_2 + \tanh kh) \tan \beta_2 k d_2 + \beta_2 (\mu_1 + \tanh kh) \tan \beta_1 k d_1 + \beta_1 \beta_2 (1 + \tanh kh) = 0 \quad (1)$$

where  $\mu_k = -\beta_k^2$ , with  $k = 1, 2$ , is the  $xx$  or  $yy$  component of the relative permeability tensor characterizing the  $k$ th YIG film. The expression

Manuscript received January 6, 1983. This work was supported by the U.S. Air Force (Rome Air Development Center) under Contract F19628-82-K-0009.

The authors are with the Department of Electrical Engineering, State University of New York at Stony Brook, Stony Brook, NY 11794.

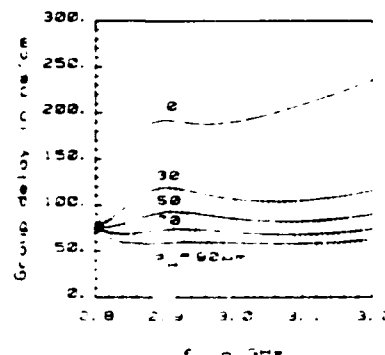


Fig. 2. Computed variation of group delay with frequency. The solid curves represent the case where the lower saturation-magnetization film ( $\mu_0 M_{0L} = 1500$  G) is closer to the ground plane and the dashed curves represent the case where the higher saturation-magnetization film ( $\mu_0 M_{0H} = 1750$  G) is closer to the ground plane. The fixed parameters in the computations are  $h = 127 \mu\text{m}$ ,  $d_L$  (thickness of lower saturation-magnetization film) = 10  $\mu\text{m}$ , and external bias field  $\mu_0 H_0 = 2500$  G. The thickness  $d_H$  of the higher saturation-magnetization film is used as a variable parameter.

for  $\mu_k$  is

$$\mu_k = (f^2 - f_{3k}^2)/(f^2 - f_{0k}^2) \quad (2)$$

where  $f_{0k} = \gamma \mu_0 H_{0k}$  and  $f_{3k} = [f_{0k}(f_{0k} + f_{Mk})]^{1/2}$  are, respectively, the lower and upper frequency bounds of the MSFVW spectrum for the individual  $k$ th film. The frequencies  $f_{0k}$  and  $f_{Mk} = \gamma \mu_0 M_{0k}$  are, respectively, the gyro- and magnetization frequencies for the  $k$ th film.

The dispersion relation (1) correctly reduces to that for MSFVW's in the single-YIG-film/dielectric/ground-plane structure in the limit of zero thickness of either film. The resulting two single-YIG-film structures have dispersion curves that are qualitatively similar but shifted in frequency. By applying the usual mode coupling criteria at the crossover points of these two sets of MSFVW single-film dispersion curves, one readily deduces the qualitative features of the MSFVW dispersion characteristics for the double-YIG-film-layered structure which are in agreement with computed characteristics. The present letter highlights only those aspects of the dispersion characteristics of MSFVW's in a double-layered structure which show that a significant improvement in nondispersive MSFVW propagation is possible utilizing such a structure rather than a single-YIG-film geometry.

The computations show that the MSFVW propagation is nondispersive over a frequency band located at the lower end of the spectrum over which the variation of MSFVW fields across both films is sinusoidal in nature, this spectrum being defined by the joint condition  $\mu_1 < 0$ ,  $\mu_2 < 0$ . This implies that a nondispersive MSFVW solution  $k$  to dispersion relation (1) exists over a band of frequencies lying immediately above the larger of the two gyro-frequencies  $f_{01}$  and  $f_{02}$ . The computations show that a bandwidth of more than 10 percent with a delay ripple of less than  $\pm 0.5$  ns may be readily achieved by an appropriate choice of parameters  $d_1$ ,  $d_2$ ,  $h$ ,  $M_{01}$ ,  $M_{02}$ , and  $H_0$ . All the computations pre-

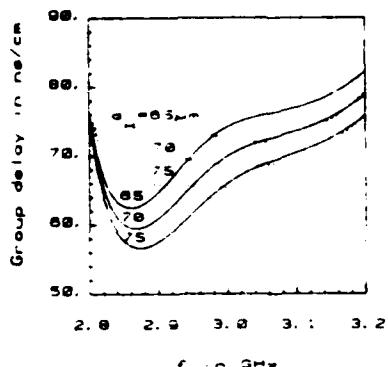


Fig. 3. Computed group-delay characteristics for fixed parameters  $h = 92 \mu\text{m}$ ,  $d_L = 10 \mu\text{m}$ ,  $\mu_0 H_0 = 2500 \text{ G}$ ,  $\mu_0 M_0 L = 1500 \text{ G}$ , and  $\mu_0 M_0 H = 1750 \text{ G}$ , with  $d_H$  used as a variable parameter. The distinction between the solid and dashed curves is the same as in Fig. 2.

sented here are for the lowest or fundamental MSFVW mode of the structure. The values of the parameters used in the computations are indicated in the captions of Figs. 2-4.

The improvement in MSFVW nondispersive propagation that results from using a double-YIG-film-layered structure is apparent in Fig. 2 where the frequency variation of group delay is presented, with the thickness of the higher saturation-magnetization film taken as a parameter. The effect on the group-delay characteristics of the saturation magnetization of the YIG film closer to the ground plane having the higher or the lower value of the two films is also shown in Fig. 2.

The difference in the group-delay characteristics resulting from whether it is the higher or the lower saturation-magnetization film that is placed closer to the ground plane is highlighted on an expanded group delay scale in Figs. 3 and 4. The computations of Fig. 3 are quasi-optimized to yield constant-delay characteristics for the case where the higher saturation-magnetization film is placed closer to the ground plane. The group-delay characteristics which obtain when, for the same parameters, the locations of the two films relative to the ground plane are interchanged are also shown in Fig. 3.

A choice of different parameters is required in order to obtain quasi-optimized constant-delay characteristics with the lower saturation-magnetization film placed closer to the ground plane (see Fig. 4). It is evident from the computations of Figs. 3 and 4 that the optimum parameters for MSFVW nondispersive propagation are changed if the locations of the two films relative to the ground plane are interchanged.

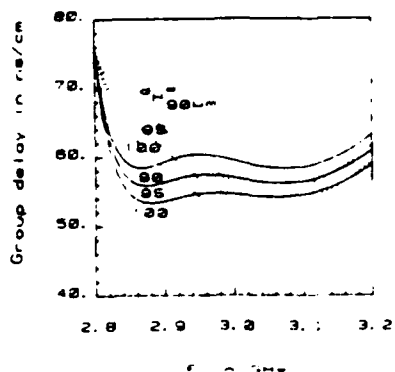


Fig. 4. Computed group-delay characteristics for fixed parameters  $h = 127 \mu\text{m}$ ,  $d_L = 10 \mu\text{m}$ ,  $\mu_0 H_0 = 2500 \text{ G}$ ,  $\mu_0 M_0 L = 1500 \text{ G}$ , and  $\mu_0 M_0 H = 1750 \text{ G}$ , with  $d_H$  used as a variable parameter. The distinction between the solid and dashed curves is the same as in Fig. 2.

In conclusion, the present computations employing readily realizable values of saturation-magnetization for the two films have shown that MSFVW nondispersive characteristics similar to those reported in [1] (where  $\mu_0 M_0$  values of 1750 and 2000 G were used) may be achieved without requiring to engage in the difficulties of growing a *low-loss* epitaxial YIG film with  $\mu_0 M_0 = 2000 \text{ G}$ . It has also been shown that the YIG film that is closer to the ground plane may have either the higher or the lower saturation magnetization of the two films but optimum parameters for MSFVW nondispersive propagation are not maintained if the locations of the two films relative to the ground plane are interchanged.

#### ACKNOWLEDGMENT

Useful comments from P. R. Emtage and M. R. Daniel who have also investigated the double-YIG-film-layered structure but in the context of linearly dispersive delay lines and with emphasis on a structure wherein the two YIG films are separated by a dielectric spacer [2] are acknowledged.

#### REFERENCES

- [1] J. P. Parekh and K. W. Chang, "MSFVW dispersion control utilizing a layered YIG-film structure," *IEEE Trans. Magn.*, vol. MAG-18, p. 1610, 1982.
- [2] M. R. Daniel and P. R. Emtage, "Magnetostatic volume wave propagation in a ferrimagnetic double layer," *J. Appl. Phys.*, vol. 53, p. 3723, 1982.

Reprinted from PROCEEDINGS OF THE  
ULTRASONICS SYMPOSIUM, Oct. 31, Nov. 1, 2, 1983

MAGNETOSTATIC-VOLUME-WAVE MODE CONVERSION  
AT A REGION OF BIAS-FIELD DISCONTINUITY\*

H.S. Tuan, J.P. Parekh and K.W. Chang

Department of Electrical Engineering  
State University of New York at Stony Brook  
Stony Brook, N.Y. 11794

ABSTRACT

The present paper reports theoretical computations of mode conversion which arises from the scattering of a magnetostatic volume wave in a YIG film, with internal bias field oriented in an arbitrary direction in the sagittal plane, at a boundary separating two regions with different bias-field orientations. A three-mode-coupling model is employed based on the assumption of a weak bias-field discontinuity. Efficient mode conversion is found to obtain for modes that are phase-matched in the direction normal to the YIG film to the incident wave. The bandwidth for mode conversion is largest when the bias field is either normal or parallel to the YIG film.

INTRODUCTION

Unlike SAW's, magnetostatic waves (MSW's) exhibit a pronounced dispersive behaviour. This feature makes MSW's more difficult to exploit for signal-processing applications. However, MSW dispersion control techniques do exist and much effort has been expended, and is currently directed,<sup>1,2</sup> at the realization of viable nondispersives as well as linearly dispersive delay lines.

The principal MSW dispersion control technique consists of placing a ground plane in proximity to the YIG film, thereby changing the MSW field profile and modifying the dispersion characteristics. Another promising approach at dispersion control is the use of a multiple-layered YIG film rather than the usual single YIG film. Theory predicts significant improvement in dispersion control when a layered YIG film is used in conjunction with a suitably spaced ground plane.<sup>3</sup>

Sethares et al.<sup>1</sup> have demonstrated that a nondispersives MSW delay line may be realized through dispersion self-compensation that is obtained by cascading two linearly dispersive MSW delay lines, one corresponding to a forward wave-type, i.e., either magnetostatic surface wave (MSSW) or magnetostatic forward volume wave (MSFVW), and the other to a backward wave-type, i.e., magnetostatic backward volume wave (MSBVW). The realization of a nondispersives delay line with acceptable performance

for some applications has recently been reported which employs a ground plane with variable spacing in the forward-wave-type (MSSW) portion of the cascaded structure and a ground plane with fixed spacing in the MSBVW portion of the structure. The variable spacing of the ground plane in the MSSW delay line is reported to provide the needed improvement in the linearity of dispersion of the delay line.

The present work is motivated by the conjecture that a monolithic implementation of the Sethares et al cascaded geometry might be possible on a single YIG film. The monolithic approach requires mode conversion from MSFVW (say) to MSBVW through the use of different bias-field orientations in the two YIG-film regions (see Fig. 1). The problem addressed in the present paper is that of determining if efficient mode conversion into a single mode is possible across a bias-field discontinuity. The problem of establishing the level of dispersion self-compensation is the same as that applying to the Sethares et al cascaded geometry and is not addressed here.

A gradual bias-field discontinuity is more realistic in practice than an abrupt bias-field discontinuity (see Fig. 2). It turns out that a gradual bias-field discontinuity is actually necessary for efficient mode conversion into a single mode. A slow change in bias-field tilt-angle and magnitude ensures that an incident fundamental-mode MSFVW is phase-matched essentially to a single converted mode, i.e., the fundamental-mode MSBVW.

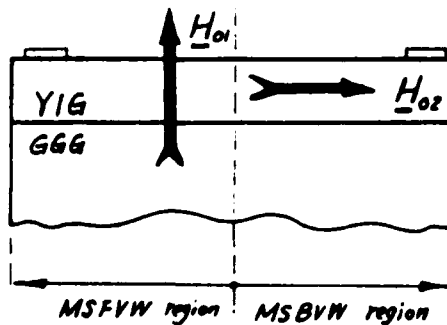


Figure 1. Abrupt bias-field discontinuity geometry.

\*Work supported by U.S. Air Force (RADC) under Contract No. F18628-82-0009

As a first step in solving the complicated problem of mode conversion across a bias-field discontinuity region, a much more basic problem which will allow a building-block approach has been solved. The two-region geometry shown in Fig. 3 is treated wherein the internal bias fields in the two regions are oriented in the sagittal plane. The building block approach will allow the present results to yield the mode-conversion properties of a gradual bias-field discontinuity region since the latter may be approximated by a number of tilted-bias-field regions, with the tilt angle changing slowly from one region to the next.

In a rigorous theory, one considers an incident magnetostatic volume wave (MSVW) to scatter into all reflected MSVW's and all transmitted MSVW's. This means that there will be an infinite set of equations in the unknown amplitude coefficients of the scattered waves. While a systematic procedure for the evaluation of these amplitude coefficients has been established which is based on an orthogonality condition between modes of a given wave-type, the real interest, of course, is in mode conversion to a single mode and not to multiple modes.

Computations show, in agreement with expectation, that mode conversion to a single mode improves with improvement in phase matching in the direction normal to the YIG film between the incident MSVW and the desired transmitted MSVW mode. This phase-matching condition implies that, the more gradual the discontinuity, the better is the accuracy in using a three-mode-coupling model which assumes a coupling of three modes, viz., the incident wave, one reflected wave and one transmitted wave.

The present work is confined in scope to the three-mode-coupling model. A weak bias-field discontinuity is assumed, with the bias field changing by a small amount, in direction only, in going through the discontinuity plane. Computed amplitude reflection and transmission characteristics are presented which demonstrate the general validity of the three-mode-coupling model provided the bias-field discontinuity is weak.

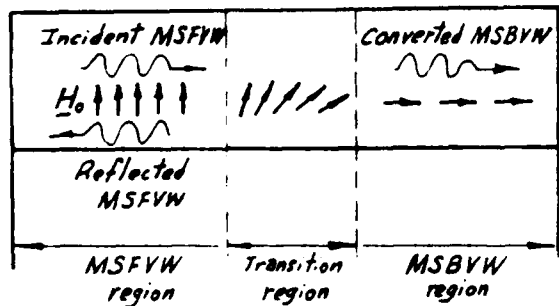


Figure 2. Gradual bias-field discontinuity geometry.

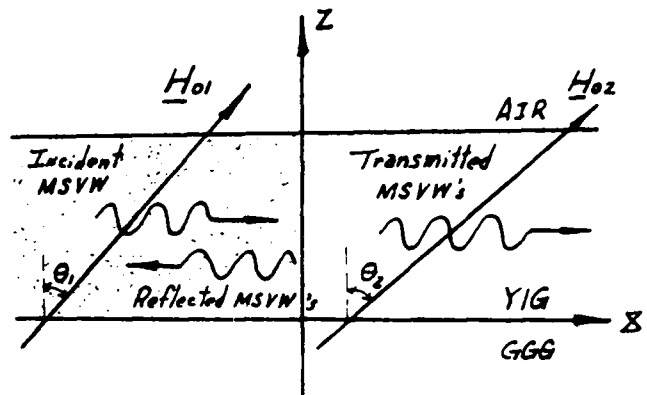


Figure 3. The mode-conversion geometry treated in this paper.

## II. MSVW'S IN A YIG FILM WITH TILTED INTERNAL BIAS FIELD

The YIG-film geometry with a tilted internal bias field lying in the sagittal plane is shown in Fig. 4. It is well-known that the YIG film supports a pure MSFW when  $\theta=0^\circ$  and a pure MSBVW when  $\theta=90^\circ$ . It has been shown by Weinberg<sup>1</sup> that, for an intermediate value of  $\theta$ , the MSVW dispersion diagram consists of two branches, one corresponding to a forward wave-type and the other to a backward wave-type. These branches meet at  $k=0$  and a frequency determined by the value of  $\theta$ . The latter frequency represents a transition between a forward wave-type and a backward wave-type, with the upper and lower dispersion branches exhibiting a resonance at the upper and lower bounds of the MSVW spectrum, respectively.

The MSVW dispersion diagrams for two neighbouring values of  $\theta$  are shown in Fig. 5. It is seen that, while in frequency bands A and C mode conversion will occur between modes of the same type (forward wave-type in band C and backward wave-type in band A), in band B mode conversion will occur between an MSFW and an MSBVW. Phase-matching is consequently expected to be good in bands A and C but poor in band B. Thus, one may expect efficient mode conversion over a wide band for values of  $\theta_1$  approaching  $0^\circ$  or  $90^\circ$  but significant difficulties in the validity of the three-mode-coupling model might occur for frequencies lying within band B. The latter difficulties do not matter much for values of  $\theta_1$  approaching  $0^\circ$  or  $90^\circ$ . However, for values of  $\theta_1$  approaching  $45^\circ$ , the frequency band B will lie somewhere near the middle of the MSVW spectrum. One might also expect difficulties in achieving phase-matching in the three-mode-coupling model for frequencies approaching the resonance frequencies where the divergence in propagation wave number  $k$  becomes large. These predictions are basically borne out by the computations.

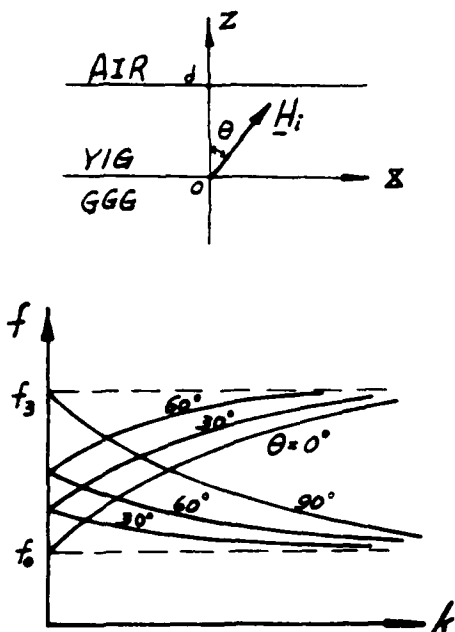


Figure 4. MSVW dispersion curves for an arbitrarily oriented bias-field in the sagittal plane.

#### 4.2. COMPUTED MODE CONVERSION CHARACTERISTICS

Computed frequency variation of the MSVW reflection R and transmission T coefficients is presented in Figs. 6 to 13 for different values of  $\theta_1$  and  $\theta_2$ . These computations are for a YIG film of thickness 20  $\mu$ m and an internal bias field magnitude of 1kG.

In Fig. 6, the incident MSVW is a pure MSVW, i.e.,  $\theta_1=0$ , and  $\theta_2$  is increased from  $2.5^\circ$  to  $10^\circ$ . This figure shows, in agreement with expectation, that R goes up as the angle discontinuity is increased. The difficulty in the validity of the three-mode coupling model at the high and low frequency bounds of the MSVW spectrum is evident in the computations where the R value becomes unacceptably large.

In Figs. 7 to 13, the value of  $\theta_1$  is increased from one figure to the next so that the entire span of values is examined. In each case, the value of  $\theta_2$  is set close to that of  $\theta_1$ , with the differential becoming smaller as  $\theta_1$  approaches the critical angle of  $45^\circ$  from either direction. The difficulty associated with band B in Fig. 5, which is somewhat alleviated by decreasing the differential angle as  $\theta_1$  approaches the  $45^\circ$  angle, is reflected in Figs. 6 to 13. A noticeable effect is that the transmission bandwidth decreases as  $\theta_1$  is increased from  $0^\circ$  to  $45^\circ$  and then increases as  $\theta_1$  is further increased from  $45^\circ$  to  $90^\circ$ . At small as well as large values of  $\theta_1$ , the transmission bandwidth is seen to be quite large. In Figs. 6 to 13, the R characteristics exhibit dips at frequencies where phase-matching is good.

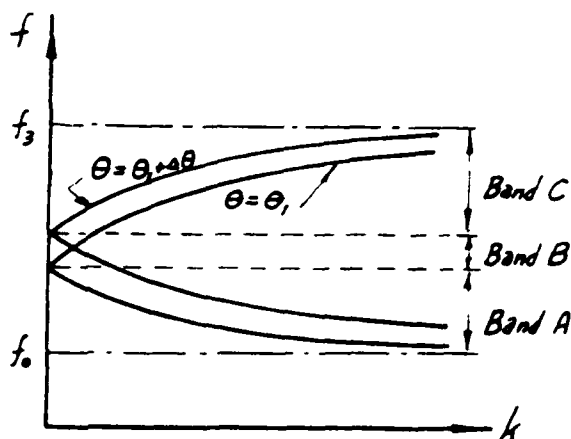


Figure 5. MSVW dispersion curves for two neighbouring bias-field angles.

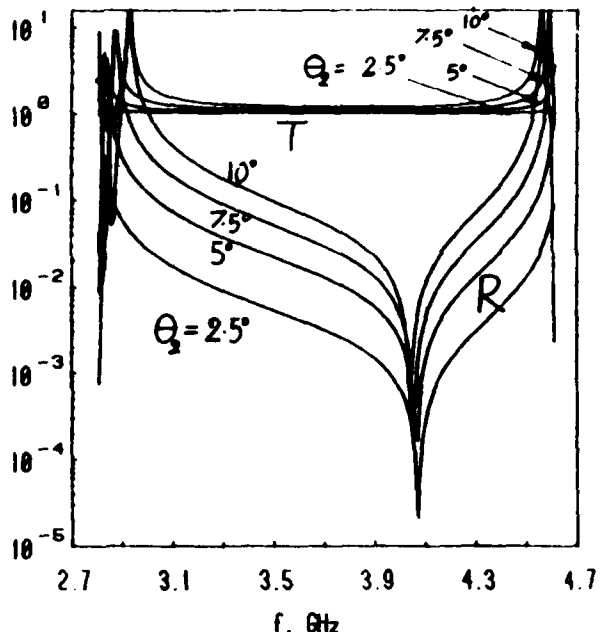


Figure 6. Frequency variation of reflection R and transmission T coefficients for fixed  $\theta_1=0^\circ$  and variable  $\theta_2$ .

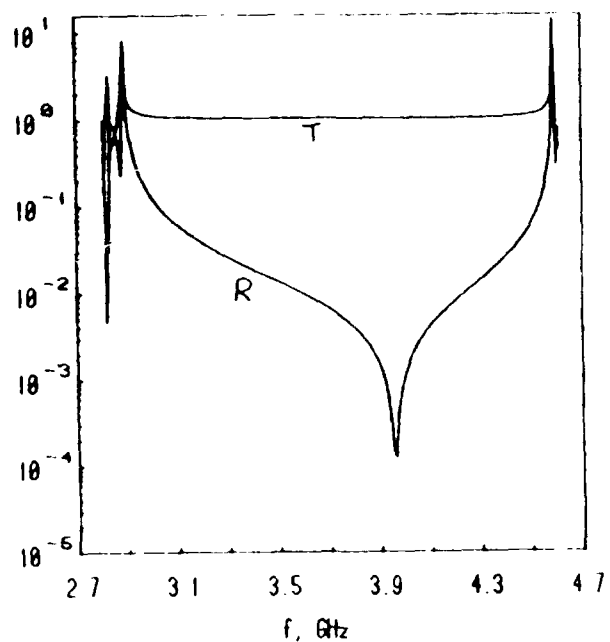


Figure 7. Frequency variation of R and T for  $\theta_1=5^\circ$  and  $\theta_2=7^\circ$ .

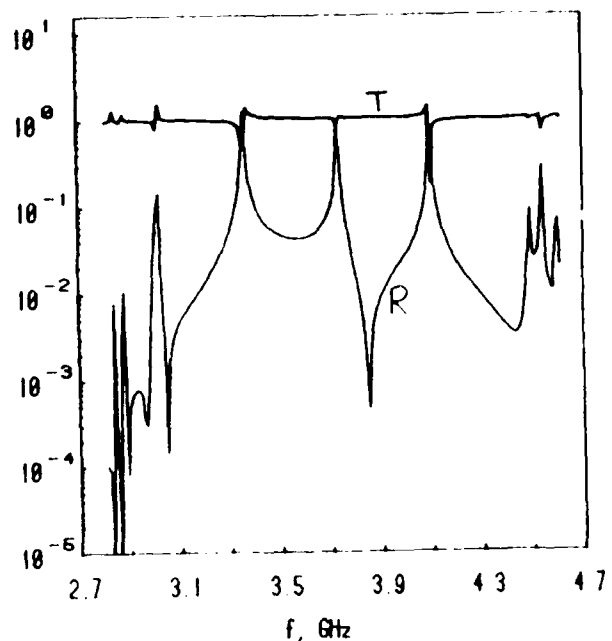


Figure 9. Frequency variation of R and T for  $\theta_1=30^\circ$  and  $\theta_2=30.3^\circ$ .

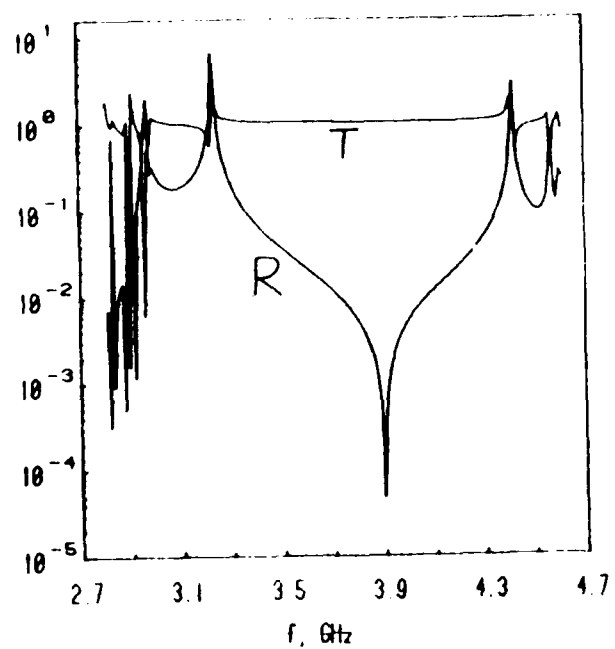


Figure 8. Frequency variation of R and T for  $\theta_1=15^\circ$  and  $\theta_2=16^\circ$ .

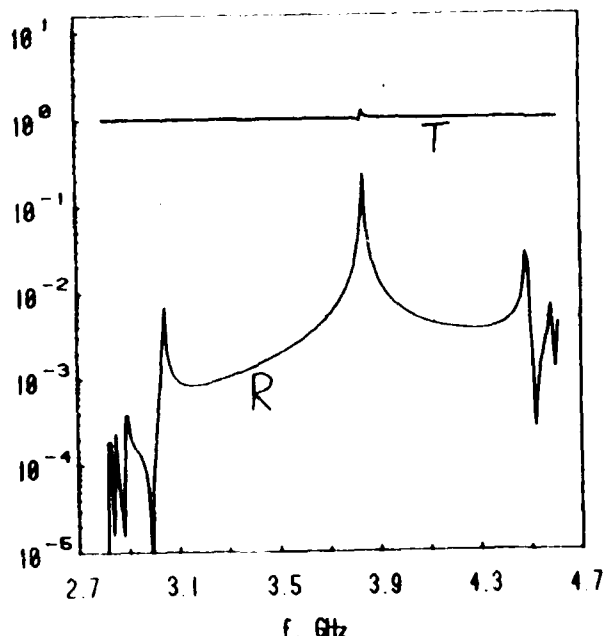


Figure 10. Frequency variation of R and T for  $\theta_1=45^\circ$  and  $\theta_2=45.1^\circ$ .

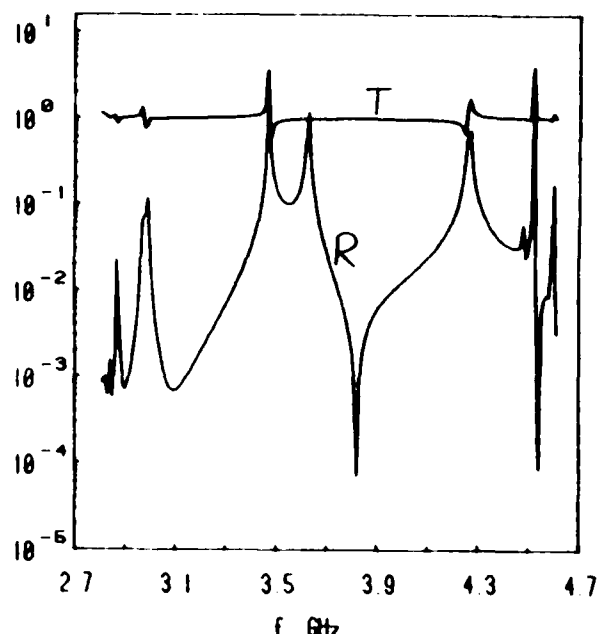


Figure 11. Frequency variation of  $R$  and  $T$  for  $\theta_1=60^\circ$  and  $\theta_2=60.3^\circ$ .

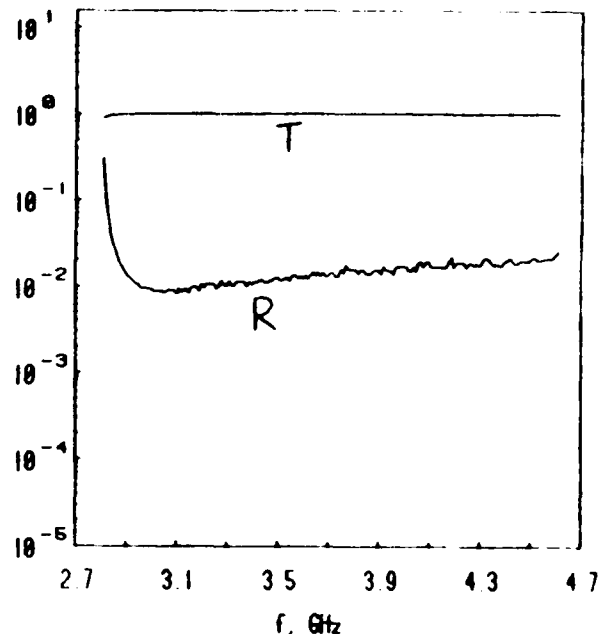


Figure 13. Frequency variation of  $R$  and  $T$  for  $\theta_1=88^\circ$  and  $\theta_2=90^\circ$ .

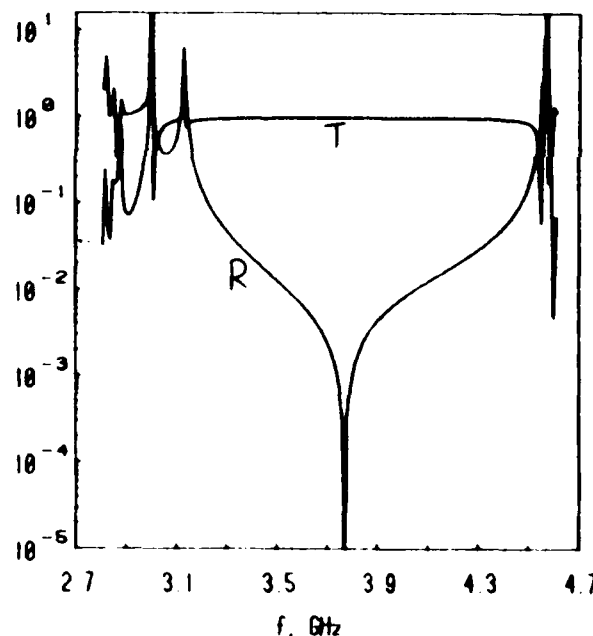


Figure 12. Frequency variation of  $R$  and  $T$  for  $\theta_1=75^\circ$  and  $\theta_2=76^\circ$ .

#### IV. CONCLUSION

The present work has demonstrated the general validity of the three-mode-coupling model provided the bias-field discontinuity is weak. If the bias-field discontinuity is not weak, the need arises to take into account more transmitted and reflected modes.

The computations have shown that efficient mode conversion obtains for modes that are phase-matched in the direction normal to the YIG film to the incident wave.

The bandwidth for mode conversion increases significantly, with a simultaneous relaxation in the need for a weak bias-field discontinuity, as the angle  $\theta_1$  approaches  $0^\circ$  or  $90^\circ$  from the critical  $45^\circ$  value. Improved bandwidth for values of  $\theta_1$  approaching  $45^\circ$  requires that the bias-field discontinuity is rendered sufficiently weak. The frequency band  $B$  of Fig. 5 where mode mismatch exists and, therefore, the need arises to take into account more modes in the coupling formalism than done here can be reduced in bandwidth through the choice of a suitably weak bias-field discontinuity but not fully eliminated.

#### REFERENCES

1. T.D. Adam et al, to appear in Special Issue on MSW's and Applications to Signal Processing of Circuits, Systems and Signal Processing.
2. I.R. Adkins, to appear in Special Issue on MSW's and Applications to Signal Processing of Circuits, Systems and Signal Processing.
3. I.P. Parekh and K.W. Chang, IEEE Trans. Magnetics MAG-19, 1868 (1983).
4. I.C. Sethares et al, Electronics Letters 16, 826 (1980).
5. I.R. Adkins et al, to be published.
6. I.J. Weinberg, in Proceedings of the 1981 RADC Microwave Magnetics Technology Workshop.

# Dielectrically induced surface waves and the magnetodynamic modes of a YIG plate

73

J. P. Parekh

## ATTACHMENT C

Department of Ocean Engineering, State University of New York Maritime College, Fort Schuyler, Bronx, New York 10465  
(Received 17 February 1975)

The magnetodynamic surface and volume modes of a YIG plate metallized at one surface are described for the case of propagation at right angles to a tangentially applied bias field. The connection of the dielectrically induced surface wave on a YIG half-space to the magnetodynamic volume modes of a YIG plate is indicated.

PACS numbers: 75.80, 84.40.S

Parekh and Ponangi<sup>1</sup> have reported the propagation characteristics of a magnetodynamic surface wave which they labeled a dielectrically induced surface wave (DISW). The choice of this nomenclature was based on the fact that this surface wave does not obtain in a magnetostatic analysis and that it also ceases to obtain in the limit  $\epsilon_{rr} \rightarrow 1$ , where  $\epsilon_{rr}$  is the relative permittivity of the YIG substrate. In this communication, we wish to point out that if, instead of the half-space geometry used in Ref. 1, a YIG plate of finite thickness is considered, the dispersion branch for the DISW becomes part of a modified TE dielectric mode dispersion curve. Thus, the latter nomenclature may actually be used in place of the nomenclature DISW. However, since the dielectric modes of a plate disappear in the limit of a half-space, the appropriateness of the nomenclature DISW is not invalidated. This distinction can be significant even though in practice one always deals with a YIG plate rather than a half-space. If a resistive absorber is placed on one surface of a YIG plate, this configuration may be more accurately modeled by a YIG half-space than by a YIG plate.

The TE magnetodynamic modes of a tangentially magnetized YIG plate have recently been reported<sup>2,3</sup> for the case of propagation at right angles to the bias field. However, the study of Gershon and Nadan<sup>3</sup> limits itself to the surface-wave modes, and thus does not bring out the relationship of the DISW to the TE magnetodynamic volume modes of a YIG plate nor to the dielectric modes to which these volume modes reduce if the spins in YIG are considered to be clamped. Furthermore, the existence of a backward-wave characteristic over part of the DISW dispersion curve pertinent to the partially metallized YIG plate geometry, wherein one surface of the YIG plate is metallized and the other adjoined to vacuum, is not indicated in Ref. 3. A brief description of the complete spectrum of the TE magnetodynamic modes of a partially metallized YIG plate is therefore given here.

Consider the YIG plate to occupy the space  $0 \leq x \leq d$ , with the surface  $x = 0$  coated with a perfectly conducting metallic film and the surface  $x = d$  adjoined to vacuum. Assuming the bias field to be oriented along the  $\hat{x}$  direction, and the guided waves to propagate along  $\hat{y}$  with the variation  $\exp[i(k_{yy}y - k_y x)]$ , the dispersion relation for the magnetodynamic modes of the YIG plate is found to be

$$\mu_{\text{eff}}[(k_y^2 - k_0^2)^{1/2} + b k_y] \tan[(k_{0y}^2 - k_y^2)^{1/2} d] + (k_{0y}^2 - k_y^2)^{1/2} = 0, \quad (1)$$

where  $k_0 = 2\pi(\mu_0 \epsilon_0)^{1/2} / f$  is the wave number of homogeneous plane waves in vacuum, and  $k_{0y} = (\epsilon_{rr} \mu_{\text{eff}})^{1/2} k_0$  is the wave number of plane waves in YIG for propagation at right angles to the bias field. The effective permeability  $\mu_{\text{eff}} = (f^2 - f_0^2) / (f^2 - f_6^2)$  is the reciprocal of the  $xx$  or  $yy$  component of the inverse of the permeability tensor characterizing the YIG medium, and  $b = j f_y / f (f^2 - f_6^2)$  is the  $yy$  (or the negative of the  $xx$ ) component of the inverse of the permeability tensor. The frequencies  $f_3$  and  $f_6$  have the expressions  $f_3 = [f_0(f_0 + f_y)]^{1/2}$  and  $f_6 = f_0 + f_y$ , with  $f_0 = \gamma \mu_0 H_0 / 2\pi$  being the gyrofrequency and  $f_y = \gamma \mu_0 M_0 / 2\pi$  the magnetization frequency.

The solution  $k_y$  of Eq. (1) for a given frequency  $f$  corresponds to a surface wave if  $k_{0y}^2 - k_y^2 < 0$  and to a volume wave if  $k_{0y}^2 - k_y^2 > 0$ . Since  $\mu_{\text{eff}}$ , or equivalently  $k_{0y}^2$ , is negative within the frequency band  $f_3 < f < f_6$ , only surface waves can obtain within this band. Outside of this band, surface waves can obtain for  $k_y > k_{0y}$  and volume waves for  $k_0 < k_y < k_{0y}$ . Equation (1) reduces correctly to the dispersion relation for the TE dielectric modes of a partially metallized dielectric plate<sup>4</sup> if the spins in YIG are considered to be clamped, i.e.,  $\mu_{\text{eff}} = 1$  and  $b = 0$ . Also, as indicated in Ref. 3, in the case of surface waves Eq. (1) reduces correctly to the dispersion relation for magnetostatic surface waves on a partially metallized YIG plate<sup>5</sup> in the short-wavelength limit  $k_y \ll k_0$ ,  $k_{0y}$ , and to the dispersion relation for magnetodynamic surface waves on an unmetallized YIG half-space<sup>1,3</sup> in the limit of a half-space, i.e.,  $d \rightarrow \infty$ . Since Eq. (1) is independent of whether the origin of the coordinate system is on the metallized or the unmetallized surface of the YIG plate, one might expect that in the limit of a half-space the surface-wave case of Eq. (1) should decouple into two dispersion relations; namely, the dispersion relation for magnetodynamic surface waves on an unmetallized half-space  $x < 0$  and the dispersion relation for magnetodynamic surface waves on a metallized half-space  $x \geq 0$ . The fact that only the former dispersion relation is obtained is simply a consequence of the result that a metallized YIG half-space does not support magnetodynamic surface waves.<sup>6</sup>

Computed dispersion diagrams for the magnetody-

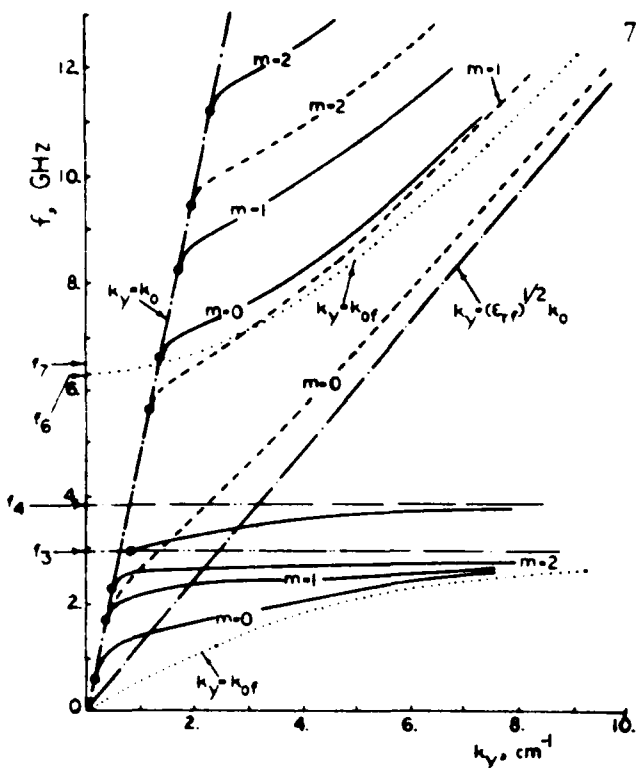


FIG. 1. Computed dispersion diagram for the magnetodynamic plate modes propagating in the  $+y$  direction with the dc bias field in the  $+z$  direction. The solid curves represent the magnetodynamic mode solutions, while the dashed curves correspond to the TE dielectric mode solutions which would obtain if the spins in YIG could be clamped. The dotted curves are the dispersion branches for plane waves in YIG propagating at right angles to the bias field. The heavy circles indicate mode cutoffs.

namic plate modes propagating in the  $\pm y$  directions are presented in Figs. 1 and 2, respectively. The computations are for a 1-cm-thick YIG plate with  $\epsilon_{r1} = 16$ ,  $\mu_0 M_0 = 1750$  G and  $\mu_0 H_0 = 500$  G. For the purpose of comparison, the TE dielectric mode solutions<sup>4</sup> for the same geometry wherein YIG is assumed to be magnetically clamped are also shown in Fig. 1. The strong effect of the spins on these dielectric modes is clearly evident in Figs. 1 and 2. The dispersion curves for the lowest three magnetodynamic volume modes corresponding to the values of the mode number<sup>4</sup>  $m = 0, 1$ , and  $2$  are shown in Figs. 1 and 2. For each value of  $m$ , where  $m = 0, 1, 2, \dots$ , two dispersion branches for the volume modes exist, one of which lies above  $f = f_1$ , and the other below  $f = f_3$ . The frequency  $f_1 = [f_0^2 + f_0 f_0 (\epsilon_{r1} - 1)^{1/2}]^{1/2}$  defines the crossing point of the dispersion curves  $k_y = k_0$  and  $k_y = k_{0f}$ . The volume modes occurring below  $f = f_3$  exhibit a resonance  $k_y \rightarrow \infty$  at  $f = f_3$ . As the frequency  $f$  is increased to  $f_3$  from below, the density of the volume modes increases monotonically, becoming infinite at  $f = f_3$ . The dispersion curves of all the volume modes, with the possible exception of the dispersion curve of the upper  $m = 0$  mode propagating in the  $-y$  direction, have cutoff frequencies on the  $k_y = k_0$  curve. The unique features of the upper  $m = 0$  volume mode propagating in the  $-y$  direc-

tion will become apparent following a description of the surface-wave branches in Figs. 1 and 2.

Only one surface-wave branch is present in Fig. 1 which corresponds to the modified magnetostatic surface wave "tied" to the YIG-vacuum interface. The wave number  $k_y$  on this branch increases monotonically from a value  $k_y = (f_0/f_M)^{1/2} k_0$  at the lower frequency bound  $f_3$ , where the slope  $df/dk_y$  (or the group velocity) is zero, to  $k_y \rightarrow \infty$  at the upper frequency bound  $f_4 = f_0 + \frac{1}{2} f_M$ . In contrast, two surface-wave branches are present in Fig. 2, one of which represents the modified magnetostatic surface wave tied to the metallized YIG surface. This branch is tangent to the dispersion curve  $k_y = k_0$  of plane waves in vacuum at the lower frequency bound  $f_3$  (which is slightly larger than  $f_3$  and is practically independent of the plate thickness), and exhibits a resonance  $k_y \rightarrow \infty$  at  $f = f_4$ . The other branch, which represents a continuation of the upper  $m = 0$  magnetodynamic volume mode and may thus be identified as a modified dielectric mode, lies within a frequency range  $f_4 < f < f_6$ , where  $f_4$  and  $f_6$  are both functions of the plate thickness. In the limit of a half-space,  $f_4$  approaches  $f_0$  from above, and  $f_6$  approaches its value for an unmetallized YIG half-space<sup>1</sup> from below. As  $d$  is decreased, a monotonic increase in  $f_4$  and a monotonic decrease in  $f_6$  take place until for a critical plate thickness  $d_{crit}$  both  $f_4$  and  $f_6$  coalesce at a frequency

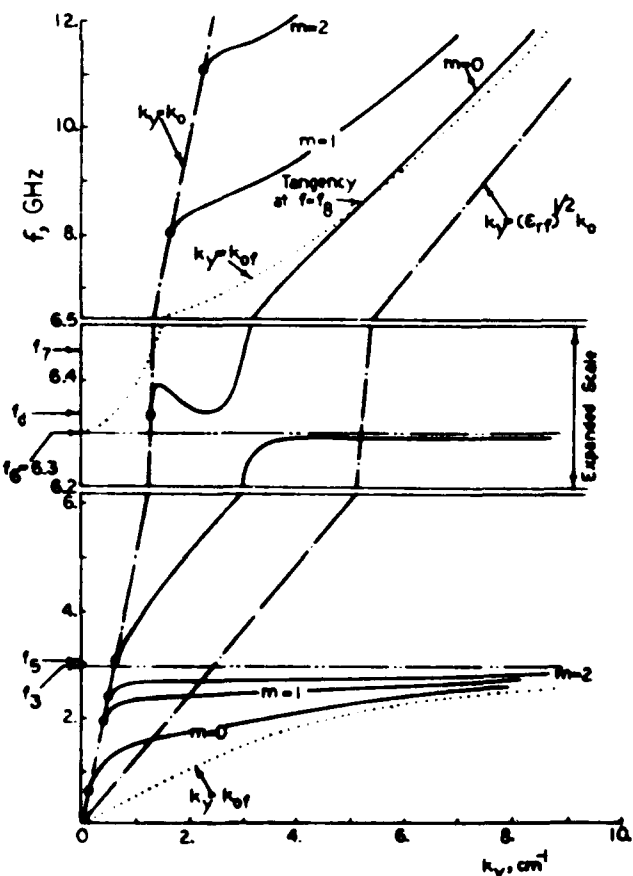


FIG. 2. Computed dispersion diagram for the magnetodynamic plate modes propagating in the  $-y$  direction with the dc bias field in the  $+z$  direction.

Fig. 10 illustrates the modified dielectric model for a forward wave.

the magnetostatic surface wave propagation disappears,<sup>6</sup> and the surface is the modified magnetostatic wave and dielectric mode surface wave in the single dispersion region of the unmetallized YIG half-

the lower  $m > 0$  curve tends to a half-  
space solution. Curves of the dielectric modes of  
the system tend to the dispersion curve  $k_y = (k_{rf})^{1/2} k_0$   
in the half-space medium, but this does  
not mean that the modes are absent since the boundary  
conditions are not satisfied in a similar fashion, the  
dielectric modes are called **dyadic volume waves**  
and the lower  $m > 0$  dispersion curve  $k_y = k_{0f}$ ,  
which is not present in the system, is an allowed solution  
in the half-space. The upper  $m > 0$  curve for  
the system has a dispersion branch now is the  
dielectric modes of the system within the frequency  
range of the leaky wave for frequencies  
above  $\omega_0$ . The boundary conditions are  
satisfied in the  $\omega > \omega_0$  region being homo-  
geneous and propagating along the

41

1100

卷之三

J. Electrostat., J. Appl. Phys., 44, 1394

Digitized by srujanika@gmail.com

1973, IEEE Trans. Microwave Theory Tech., Vol. 21, No. 1, Jan. 1973.

Author: Guided Waves McGraw-Hill,

56-5443-2-25-1

Further analysis indicates the existence of a solution in the half space, this solution being of opposite sign, exact magnitude, and displacement current into

MISSION  
of  
Rome Air Development Center

RADC plans and executes research, development, test and selected acquisition programs in support of Command, Control Communications and Intelligence (C<sup>3</sup>I) activities. Technical and engineering support within areas of technical competence is provided to ESD Program Offices (POs) and other ESD elements. The principal technical mission areas are communications, electromagnetic guidance and control, surveillance of ground and aerospace objects, intelligence data collection and handling, information system technology, solid state sciences, electromagnetics and electronic reliability, maintainability and compatibility.

ENVID

DATE

3-88

DTIC